A Membrane-Disruptive Action of VBIT-4 Challenges Its Role as a Widely Used VDAC1 Oligomerization Inhibitor

Varun Ravishankar[1#], Luís Borges-Araújo[2,3#], Megha Rajendran[4#], Elodie Lafargue[5], Deborah Byrne[6], Nicolas Buzhinsky[5], Mya S. Wolfe[4], Wendy Fitzgerald[4], Nina A. Bautista[4], Bethel G. Beyene[4], Motahareh G. Larimi[4], Jean-Pierre Duneau[1], James Sturgis[1], Sergey M. Bezrukov[4], Ignacio Casuso[5], Tatiana Rostovtseva[4], Lucie Bergdoll[1*]

1. Laboratoire d'Ingénierie des Systèmes Macromoléculaires, CNRS, UMR 7255 - Aix Marseille Université, 31 Chemin Joseph Aiguier, 13402 Marseille, France. 2. Laboratoire de Biologie et Modélisation de la Cellule, CNRS, UMR 5239, Inserm, U1293, Université Claude Bernard Lyon 1, Ecole Normale Supérieure de Lyon, Lyon, France. 3. Centre Blaise Pascal de Simulation et de Modélisation Numérique, Ecole Normale Supérieure de Lyon, Lyon, France. 4. *Eunice Kennedy Shriver* National Institute of Child Health and Human Development, NIH, Bethesda, Maryland, 20892, USA. 5. U1325 Aix-Marseille Université, INSERM, DyNaMo, Turing Centre for Living System, Marseille, France. 6. Biomass & Protein Engineering Aix Marseille Université, CNRS, IMM FR3479, 13402, Marseille, France.

# : equal contribution

*corresponding author : Lucie Bergdoll

Email: lbergdoll@imm.cnrs.fr

Competing Interest Statement: The authors have no competing interests.

Keywords: VBIT-4, VDAC, membrane destabilization, lipid pores, toxicity

Abstract:

VDAC, the most abundant protein in the outer mitochondrial membrane, plays a central role in mitochondrial physiology. Its oligomerization has been considered to be involved in critical processes, such as mitochondrial DNA release and apoptosis; yet, the underlying molecular mechanisms remain poorly defined. VBIT-4, a small molecule widely regarded as a VDAC1 oligomerization inhibitor, has seen extensive applications over the past five years without proper mechanistic characterization. Using high-speed atomic force microscopy, we directly visualized VDAC1 oligomerization in planar lipid membranes and examined the effects of VBIT-4. Unexpectedly, we discovered that VBIT-4 partitioned into lipid bilayers at micromolar concentrations and disrupted membrane structure irrespective of VDAC1's presence. Complementary approaches—including single-channel electrophysiology, microscale thermophoresis, and coarse-grained molecular dynamics—corroborated VBIT-4 strong membrane partitioning and destabilizing activity, while showing no detectable effect on VDAC1 or its clustering. Consistent with this behavior, VBIT-4 induced VDAC1-independent cytotoxicity in HeLa cells at concentrations above 10 µM. Together, these findings demonstrate that VBIT-4 acts by perturbing lipid bilayers and promoting membrane defects rather than by inhibiting VDAC1 oligomerization. Thus, providing an alternative mechanism of action for interpreting studies using VBIT-4 underscores the need to consider its potent, nonspecific membrane activity in cells.

Teaser: Once thought to block VDAC1 oligomerization, VBIT-4 instead acts independently of VDAC1 as a membrane-active compound that destabilizes and permeabilizes lipid bilayers.

Introduction

The Voltage-Dependent Anion Channel (VDAC) is the most abundant protein of the mitochondrial outer membrane (MOM), accounting for over half of its protein content[1, 2]. As the primary conduit between mitochondria and cytosol, it mediates ATP/ADP and ion fluxes, thereby playing a central role in energy metabolism. Beyond transport, VDAC also regulates diverse mitochondrial functions, including apoptosis[3, 4], and calcium homeostasis[5–7]. Mammals express three isoforms (VDAC1, 2, and 3), which share their channel transport function but diverge in interaction partners and pathway specificity[8, 9].

VDAC is often recognized as a drug target because of its links to diverse diseases[10–12]. Yet its essential roles in physiology, lack of a defined catalytic site[12], and incomplete understanding of its functions in vivo complicate therapeutic development. One proposed strategy, attracting increased interest in recent years, is to target VDAC oligomerization implicated in essential physiological functions, including mitochondrial DNA release[13], lipid scrambling[14], mitochondrial organization[15], and interaction with MOM proteins[16] — processes central to mitochondrial dynamics and stress adaptation. VDAC has been shown by different groups to form oligomers that are heterogeneous lipid–protein clusters rather than discrete complexes[1, 2, 17, 18], which challenges their selective targeting.

In 2016, Ben-Hail *et al.* introduced VBIT-4 as a small-molecule inhibitor of VDAC1 oligomerization[19]. Since then, it has been widely used to probe VDAC1 in various diseases, ranging from autoimmunity and neurodegeneration to metabolic disease models[13, 20–25]. Despite this broad use, the mechanism of action of VBIT-4 remains unclear.

High-speed atomic force microscopy (HS-AFM) has recently enabled real-time, nanometer-scale visualization of VDAC1 oligomerization[17], showing that lipid composition is a key regulator and that disruption of physiological lipid distribution destabilizes native-like assemblies. Using HS-AFM, we examined the effects of VBIT-4 on VDAC1 oligomerization and found that, unexpectedly, it caused membrane permeabilization and bilayer defects even in the absence of VDAC1. Then, using complementary methods—including single-channel electrophysiology, microscale thermophoresis, and molecular dynamics—we confirmed that VBIT-4 partitions into membranes and perturbs bilayer properties independently of VDAC. Cellular assays corroborated these findings by showing that VBIT-4 induces cytotoxicity above 10 μM and mitochondrial dysfunction below 10 μM. These findings suggest an alternative mechanism of action of VBIT-4 and underscore the importance of systematically assessing drug–membrane interactions early in the drug development process.

Results

VBIT-4 induces perturbations in VDAC1-containing membranes

HS-AFM provides label-free, real-time imaging of nanoscale membrane dynamics under near-physiological conditions, making it well-suited for assessing small molecule effects on VDAC1 oligomerization. We applied this approach to POPC:POPE:cholesterol membranes, reconstituted

with or without VDAC1 and adsorbed on mica. Before VBIT-4 addition, VDAC1-containing membranes showed the characteristic "honeycomb" topography[17] (**Figure 1A,E**) , with extended protein assemblies separated by lipid-rich zones. Addition of 1 μM VBIT-4 produced small perforations a few nanometers wide and deep (**Figure 1B***), indicating local bilayer destabilization without affecting VDAC1 clusters (**Figure 1F**). Height profiles clearly distinguished VDAC1 from deeper VBIT-4–induced defects. At 10 μM, the number and size of defects increased (**Figure 1C***). AFM images revealed a clear difference between organized VDAC1 pores, which remained intact, and the irregular defects formed in lipid regions by VBIT-4 (**Figure 1G**). Height profiles analysis confirmed that VBIT-4-induced pores are wider (10-20 nm) and deeper (3-4 nm) than those of VDAC1 (5-7 nm wide, 0.8-2.5nm deep). The lack of structural changes in VDAC1 clusters indicates that VBIT-4 targets the lipid matrix rather than the protein assemblies. Height distribution analysis (**Figure 1D**) shows that VDAC1 membranes without VBIT-4 yield a narrow peak around –1nm, whereas addition of VBIT-4 broadens the distribution to -4 nm at 1 μM and up to -5.5 nm at 10 μM, reflecting heterogeneous pore formation.

VBIT-4 induces membrane perturbation in protein-free lipid bilayers

To assess the direct effects of VBIT-4 on lipid membranes, we examined protein-free membranes using HS-AFM. Control bilayers displayed uniform topography without defects (**Figure 1I**). Addition of 1 μM VBIT-4 induced isolated protrusions (**Figure 1J**) up to tens of nanometers in diameter (**Figure 1J** inset), consistent with higher-order oligomers or aggregates. Coarse-grained simulations support formation of VBIT-4 micelles (**Figure 1H**, Supplementary Figure 1) rather than monomers (VBIT-4 is rod-shaped ~2 nm × 0.5 nm when neutral and ~1.2 nm × 0.5 nm when charged), consistent with the observed protrusions. At 5 μM, deformations intensified, producing transmembrane defects (**Figure 1K**); at 50 μM—commonly used in cell studies—disruption was pronounced, and at 100 μM HS-AFM revealed nanometer-scale perforations consistent with rupture (**Figure 1L,M**). Height profiles analysis confirmed a progressive increase in defects dimensions: mean defect depth increased from 2.5-3 nm at 50 μM (**Figure 1L inset**) to 4.5 nm at 100 μM VBIT-4 (**Figure 1M inset**) while average defect diameters expanded from ~20 nm to ~50 nm over the same concentration range, demonstrating a dose-dependent destabilization of the lipid bilayer by VBIT-4. Thus, VBIT-4 alone progressively destabilizes membranes in a concentration-dependent manner, culminating in structural failure at high concentrations. Notably, defects appeared at lower concentrations in the presence of VDAC1, likely reflecting its lipid-scrambling activity[14], which may accelerate VBIT-4 transfer between leaflets and promote pore formation.

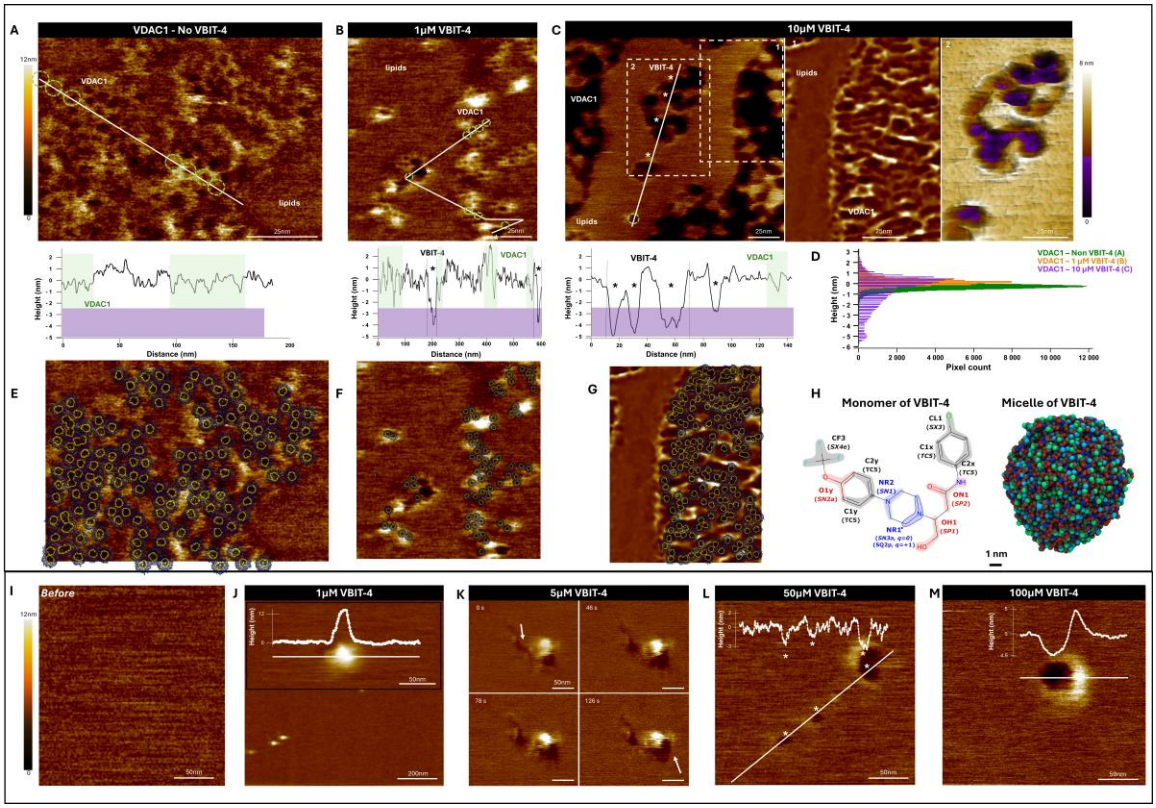

Figure 1. VBIT-4 induces defects in membrane bilayers, independently of VDAC1 presence. Upper panels: VDAC1 reconstituted into POPC:POPE:chol (60:32.5:7.5) liposomes was adsorbed onto a mica surface for AFM imaging. AFM image and associated height profile before (**A**) and after addition of 1µM (**B**) and 10 µM (**C**) VBIT-4 to lipid bilayers deposited on mica in the presence of VDAC1. The purple rectangles of the height profiles indicate the 2.5 nm threshold: values above this limit correspond to pores formed by VDAC1 (green circles), whereas values below correspond to openings induced by the VBIT-4 molecule. Asterisks (*) denote VBIT-4–induced pores, and selected VDAC1 locations are highlighted with green circles. **C.** AFM images showing the effect of VBIT-4 (10 µM) on membrane-embedded VDAC1. **Left:** overview of the membrane surface with VDAC1 pores and VBIT-4–induced openings. **Middle:** Section (1) shows a zoomed-in high-resolution AFM images revealing the honeycomb-like structure of VDAC1 (Fourier filter). **Right:** Section (2) 3D zoomed view illustrating the depth of the pores/openings. **D.** Quantitative pore size distribution derived from pixel depth/height analysis of the overview images shown in A, B, and C. Histograms represent the distributions without VBIT-4 (green, panel A), in the presence of 1 µM (orange, panel B) or 10 µM (purple, panel C) VBIT-4. **E. F. G.** are computer models derived from AFM images in A, B, and C, respectively (see Methods and[17]). VDAC1 is depicted as a dark solid surface, with the first lipid shell in yellow, and the other interstitial lipids in an atom color-coded representation. **H.** Monomer and micellar structure of VBIT-4 obtained by molecular dynamic simulations (see Methods and below). On the monomer structure, polar groups are highlighted in red, slightly hydrophobic in grey, and strongly hydrophobic in blue. **Bottom panels:** Membrane was adsorbed onto a mica surface for AFM imaging. **I.** The AFM image of a lipid membrane (without VDAC) on a mica substrate shown before the injection of the VBIT-4 molecule. Addition of VBIT-4 at different concentrations: 1 µM (**J**), 5 µM (**K**), 50 µM (**L**), and

100 μM (**M**). The insets show the height profiles. The height of the false-colour scale in all images was 12 nm.

VBIT-4 induces membrane defects

To confirm membrane perturbation, we performed Laurdan fluorescence measurements in PC:PE:chol (62.5:30:7.5) liposomes. VBIT-4 induced a dose-dependent decrease in generalized polarization (GP), consistent with increased water penetration and lipid disorder (**Figure 2A**, **Supplementary Figure 2**). To further assess VBIT-4–induced membrane permeabilization, we performed a fluorescein leakage assay using large unilamellar liposomes of the same composition as in the Laurdan fluorescence experiments. At high internal concentrations, fluorescein self-quenches, whereas its release upon membrane disruption increases fluorescence due to dequenching. The addition of VBIT-4 triggered a gradual and concentration-dependent increase in fluorescence (**Figure 2B**), indicating progressive leakage consistent with membrane destabilization by the compound.

To assess functional consequences of VBIT-4 insertion, we recorded currents across planar lipid membranes (PLMs) using the conventional voltage-clamp mode. VBIT-4 increased membrane conductance in a clear concentration-dependent manner, with rupture typically occurring between 20–50 μM across all lipid compositions tested—PC:PE:chol, soybean polar lipid extract (PLE), and DPhPC—despite experiment-to-experiment variability (**Figure 2C,D**; **Supplementary Figure 3A**; Supplementary Table 1). Representative traces illustrate progressive conductance increases, reaching ~3.5 nS at 30 μM in PC:PE:Chol and ~5 nS at 25 μM in PLE shortly before rupture (**Figure 2C,** red arrow, **Figure 2D**; **Supplementary Figure 3A**). Large current fluctuations typically preceded rupture, consistent with the formation of heterogeneous lipidic pores[26–28] rather than uniform channels. Similar behavior has been reported for various amphiphilic compounds, which typically produce noisy current traces without well-defined discrete conductance levels[29–32]. VBIT-4–induced defects displayed nearly linear, symmetric current–voltage relationships (Inset in **Figure 2B** and **Supplementary Figure 3B**). These results demonstrate that VBIT-4 causes nonspecific membrane permeabilization above ~15 μM. Our results differ from the original report[19], where 40 μM VBIT-4 did not permeabilize membranes formed by the 'painted' bilayer method using organic solvent. In contrast, when we repeated experiments with painted membranes (Orbit mini system), VBIT-4 induced leakage starting from 5 μM (**Supplementary Figure 3C**), consistent with its effects in solvent-free PLMs. Together, these data demonstrate that VBIT-4 partitions into bilayers and disrupts their structure in a concentration-dependent manner, independently of VDAC.

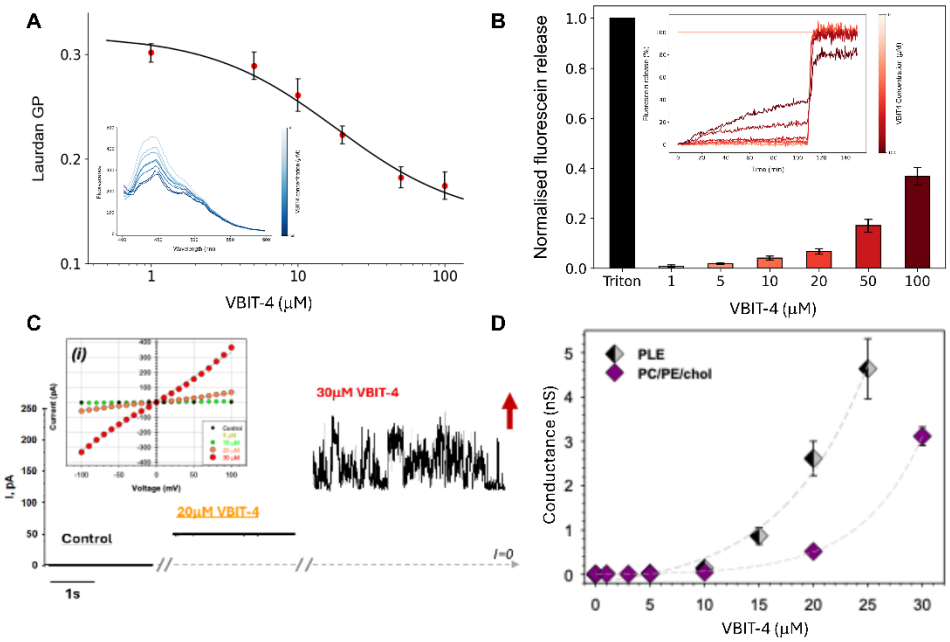

Figure 2. VBIT-4 incorporates into lipid membranes. A. Laurdan GP analysis of PC:PE:chol (62.5:30:7.5) liposomes with VBIT-4. The plot shows a VBIT-4 concentration-dependent decrease in laurdan generalized polarization (n=5). The inset corresponds to the fluorescence spectra at VBIT-4 concentrations changing from 0 (light blue) to 100 μM (dark blue), the inset data can be found at a larger scale in Supplementary Figure 3. **B.** Liposome leakage test of encapsulated fluorescein sodium salt from PC:PE:chol (w:w 62.5:30:7.5) liposomes with increasing concentration of VBIT-4 and TX-100 (0.5 %). The inset represents the kinetics of fluorescein leakage from the liposomes. **C.** Representative current traces obtained on the same PLM made from PC:PE:chol (60:32.5:7.5) before and after consequent additions of 20 and 30 μM of VBIT-4 to the *cis* compartment of the chamber at 80 mV of applied voltage. Large fast fluctuations of the membrane conductance at 30 μM of VBIT-4 preceded the membrane rupture shown by the upward red arrow. The inset shows the current-voltage (I/V) curves obtained in the experiments at different VBIT-4 concentrations. Grey lines are linear regressions indicating the nearly Ohmic behavior of VBIT-4-induced conductances. Dashed grey lines show a zero current. The membrane-bathing solutions consisted of 150 mM KCl buffered with 5 mM HEPES at pH 7.4. The current was digitally filtered using a 500 Hz Bessel (8-poles) filter for presentation. **D**. Conductance of planar membrane increases with VBIT-4 concentration. PLM were made from PC/PE/chol as in (C) and from PLE as in Supplementary Figure 3A. Membrane conductance was calculated from the corresponding I/V curves. The dashed lines are an exponential fit to guide the eye. Error bars are ±SD from measured conductances at different voltages.

VBIT-4 does not affect VDAC1 channel properties

To test whether VBIT-4 alters VDAC1 conductance or voltage-gating, we performed single- and multichannel recordings at 5–30 μM VBIT-4. Unlike Ben-Hail et al.[19], we observed no irreversible changes in VDAC1 conductance or gating across eight experiments (**Figure 3A, B**). Instead, VBIT-4 caused a dose-dependent increase in overall membrane conductance (**Figure 3A**), leading to membrane rupture, which is consistent with the nonspecific leakage observed in protein-

free membranes (**Figure 2C**). Multichannel recordings confirmed that open probability (P_{open}) was unchanged (**Figure 3B**).

To further probe VBIT-4's interaction with VDAC1, we used complementary biophysical approaches. Microscale thermophoresis (MST), a sensitive technique for detecting molecular interactions in solution**,** was applied to lipid nanodiscs. VBIT-4 titrated into lipid nanodiscs produced a Temperature-Related Intensity Change (TRIC) fluorescence signal (**Figure 3C**) with an average apparent dissociation constant (k_D) of ~70 µM, comparable to reported affinities for VDAC1 in detergent micelles[19, 33]. An equivalent signal in VDAC1-containing nanodiscs, but with a higher k_D of 260 µM can be explained by the lower amount of lipids in the nanodiscs due to the space occupied by VDAC1. This indicates non-specific partitioning of VBIT-4 into the bilayer rather than interaction with VDAC1 (**Figure 3C**). Furthermore, no spectral shift in the fluorescence ratio of 670nm/650nm was observed—this was expected for a specific ligand inducing changes in the chemical environment of the target—confirming the absence of any detectable interaction with VDAC1, while no signal was detected in controls lacking lipids (**Supplementary Figure 4A** and **4B**). The variability across replicates, also seen in published titrations[19, 33], further supports partitioning into the bilayer rather than binding to a defined protein site. The previously reported affinity likely reflects VBIT-4 partitioning into the hydrophobic core of detergent micelles[19, 33]. Thus, VBIT-4 increases bilayer permeability independently of VDAC1 and does not affect intrinsic channel properties.

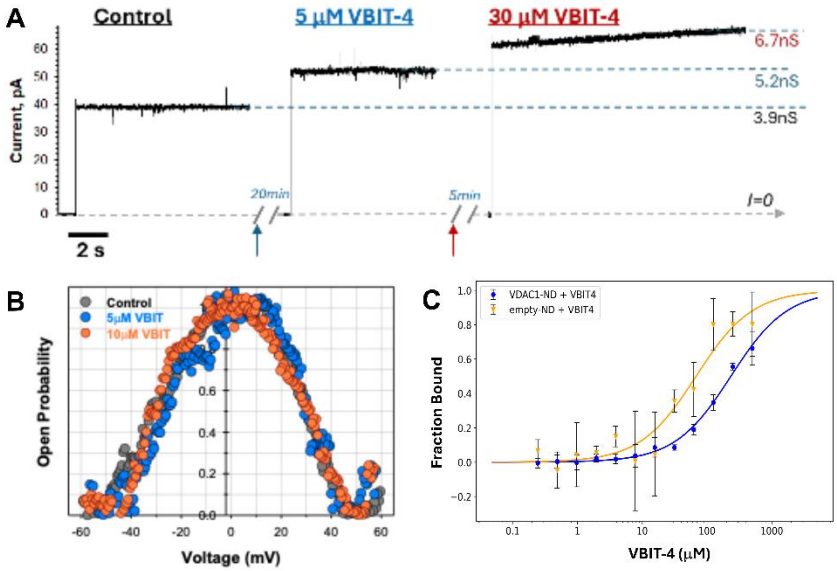

Figure 3. VBIT-4 destabilizes lipid membranes independently of VDAC1. A. Representative single-channel current traces obtained with VDAC1 reconstituted in PLM formed from PLE before (control) and after the addition of 5 and 30 µM VBIT-4 to the *cis* compartment. Addition of VBIT-4 and the time of the recordings after additions are indicated by upward arrows. The jumps in the current correspond to the application of 10 mV voltage following the application of 0 mV. The record was obtained on the membrane with the same single channel of 4 nS conductance as in the control. The grey dash line indicates zero current (*I=0*). The dashed blue lines indicate the current through the open single channel.

Addition of 30 μM VBIT-4 induced a monotonic increase of membrane conductance, leading to membrane rupture. Current records were digitally filtered using an averaging time of 0.2 ms. **B.** Characteristic bell-shaped plots of open probability as a function of the applied voltage obtained in a multichannel experiment with VDAC1 in a PLE membrane in control and after addition of 5 and 10 μM VBIT-4. In all panels, the membrane-bathing solutions consisted of 1 M KCl buffered with 5 mM HEPES at pH 7.4. **C.** Binding of VBIT-4 to fluorescently labeled VDAC1 into nanodiscs (blue) or to empty nanodiscs, with MSP1D1 labeled (yellow), monitored by microscale thermophoresis. The plot shows normalized fluorescence at 650 nm measured 2.5 s after IR-laser activation across increasing VBIT-4 concentrations. An average apparent $K_d$of 70 μM with a confidence intervalle from 20-167 μM (n = 4) was obtained for VBIT-4 binding to empty nanodiscs and 234 μM with a confidence intervalle from 105-331 μM (n = 2) for VDAC1-containing nanodiscs.

Mechanistic insights into VBIT-4–mediated lipid bilayer destabilization from coarse-grained simulations

Having shown that VBIT-4 partitions into membranes and disrupts its integrity independently of VDAC1, we turned to molecular dynamics (MD) simulations to explore the mechanism. To reach longer timescales and larger system sizes, we used coarse-grained (CG) simulations with the Martini 3 force field[34], which reliably models membrane dynamics and small-molecule interactions, including with VDAC[35, 36].

A CG model of VBIT-4 was parameterized from all-atom simulations (**Figures 4A and 4B**). Considering that VBIT-4 can exist in neutral and protonated states with distinct conformations, we developed separate models to analyze their effects (see Methods).

VBIT-4 readily inserts into lipid bilayers

Unbiased MD simulations show that VBIT-4 spontaneously inserts into lipid bilayers, consistent with its hydrophobic nature (**Figures 4C and 4D**). The $\log P_{(oct/water)}$ scale measures a molecule's hydrophobicity, with values below 0 indicating polar, water-soluble molecules (e.g., glucose, logP ~ -3.2[37]), and values above 0 indicating apolar, lipophilic molecules (e.g., cholesterol, logP > ~ 8[38]). Its predicted logP of ~3.5 (**Figure 4E**), similar to ibuprofen (logP ~ 3.9[39]), indicates strong membrane partitioning; a 1 μM aqueous concentration corresponds to ~3.5 mM in the bilayer, highlighting its lipid preference. Simulations also revealed a tendency to self-aggregate into micelle-like clusters regardless of the charge state (**Supplementary Figure 1**). These findings are consistent with Fourier-transform infrared spectroscopy (FTIR) measurements showing that VBIT-4 exists predominantly as aggregates, with only a minor soluble fraction (**Supplementary Figure 5**).

To determine whether VBIT-4 can translocate across biological membranes—which is required in cells to reach the mitochondrial membranes—we performed umbrella sampling simulations to compute the Potential of Mean Force (PMF), which quantifies the free energy profile along the translocation pathway. As expected, the neutral form of VBIT-4 has a significantly lower translocation barrier (~30 kJ/mol) compared to the charged form (~55 kJ/mol, **Figure 4C**). While relatively high, these barriers are compatible with passive translocation, especially under conditions of elevated local concentration, membrane defects, transient pores, or lipid-scrambling activity, as suggested by our AFM experiments (**Figure 1**). It is important to note that the energy barrier estimated here applies to a single VBIT-4 molecule and does not account for cooperative or

concentration-dependent effects. Overall, VBIT-4 not only partitions into the membrane but also has the potential to translocate across it.

VBIT-4 partitions into lipid membranes and induces membrane destabilization

We simulated a mitochondrial outer membrane mimic at increasing VBIT-4 concentrations (1:16–1:1.5 VBIT-4:lipid). A recent predictor[40] estimates the pKa of VBIT4 to be between 5.7 and 6.9, consistent with the known piperidine pKa[41]. Because this range, close to physiological pH, allows coexistence of neutral and charged states, we simulated 50:50 mixtures, which produced pore-like aggregation and destabilization intermediate between the two extremes (**Figure 4F, G-L**). We also simulated both neutral and charged states of VBIT-4 independently (**Supplementary Figure 6**, **Figure 4G-L**). In all cases, VBIT-4 spontaneously inserted into the bilayer, increasing area per lipid, decreasing thickness and order, and enhancing water permeability (**Figure 4G-L**). At high concentrations, a neutral and 50:50 mixture of VBIT-4 aggregated to form pore-like structures that promoted lipid flip-flop and tail protrusion (**Figure 4G-L**). Charged VBIT-4 did not form stable pore-like structures but markedly increased permeability. Notably, the CG-Martini force field is known to over-stabilize membranes [42], suggesting that any observed destabilizing effects likely underestimate the actual impact on biological membranes. Despite this, the phase-separation and pore-like structures observed here are consistent with AFM and electrophysiology, supporting a mechanism in which VBIT-4 destabilizes bilayers at micromolar concentrations.

VBIT-4 facilitates polar defects formation in lipid bilayers

To assess how VBIT-4 destabilizes membranes, we calculated the energy required to form polar defects—transient water-filled disruptions of the hydrophobic core. The energy required to form such defects determines membrane stability, with higher barriers preventing disruption and lower barriers making the membrane more susceptible to perturbation. To this end, we utilized the pore-formation reaction coordinate developed by Jochen Hub and applied umbrella sampling to probe this effect[43]. Control simulations without VBIT-4 yielded high barriers (~250 kJ/mol) due to the known overstabilization of Martini 3, whereas all-atom DPPC simulations typically report ~50 kJ/mol.

At ~1:3 VBIT-4:lipid ratios, both charged and neutral VBIT-4 reduced the barrier by ~60–100 kJ/mol (Figure 3M,N), indicating that the compound facilitates defect formation despite inflated absolute values in Martini. Although the small system size limited pore-like aggregation, unbiased simulations confirmed increased area per lipid, reduced thickness, enhanced water permeability, and frequent tail protrusions and flip-flop events—all consistent with reduced bilayer stability. Hence, even at low concentrations, VBIT-4 impacts the properties of biological membranes, independently of VDAC.

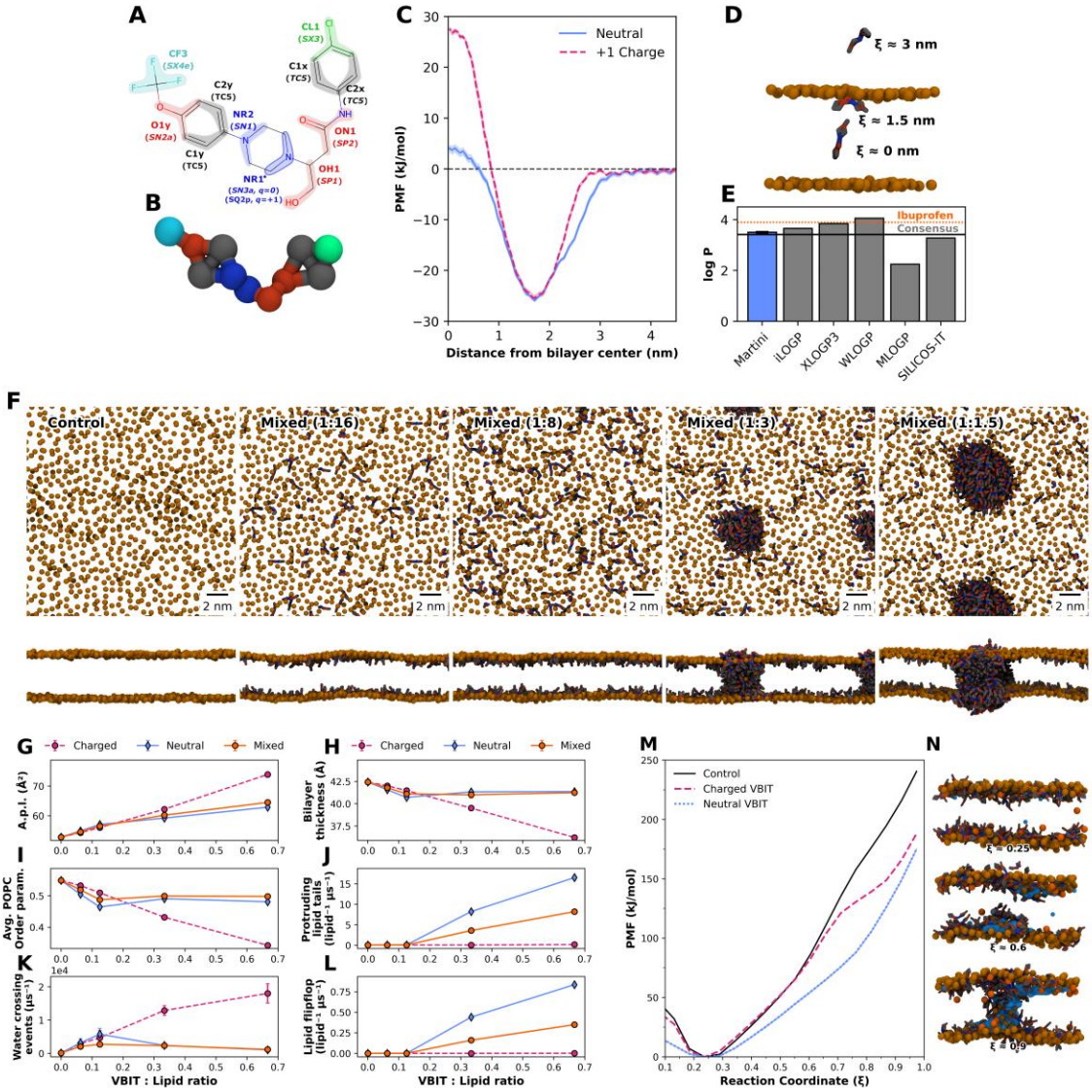

Figure 4. VBIT-4 partitions into lipid bilayers and disrupts membrane integrity through pore-like structures. A. VBIT-4 chemical structure and Martini 3 model mapping. Atom-to-bead mappings are indicated by the coloured shapes. Assigned Martini 3 bead names are indicated for each bead as overlaid bold text, with the corresponding bead types in italic text. Protonable group is highlighted (⋆). **B.** VBIT-4 Martini 3 CG model. **C.** Potential of Mean Force (PMF) of VBIT-4 insertion into coarse-grained MOM membranes. Free energy profiles are shown for both the neutral (blue) and protonated (+1 charge, red) forms of VBIT-4. **D.** Snapshots of the insertion of neutral VBIT-4 at different distances from the bilayer center (ξ); lipid PO_4 beads are represented in orange, and VBIT-4 in grey/red/blue. **E.** Predicted octanol–water partition coefficient (Log P) values for VBIT-4. VBIT-4 hydrophobicity was estimated using several computational predictors (grey) and the Martini 3 coarse-grained model developed in this study (blue). Higher Log P values indicate greater lipid solubility. The dashed black line shows the consensus value across predictors, while the orange dashed line marks the Log P of ibuprofen (~3.9), a well-known hydrophobic drug used here for comparison. **F.** Representative snapshots showing the impact of increasing VBIT-4 concentrations on MOM membrane mimics after 10 µs of CG MD simulation. (Lipid phosphate beads are shown in orange; VBIT in grey, with

chemically distinct beads highlighted in red and blue). Top and side snapshots are shown for a 50:50 mix of charged and neutral VBIT-4 at increasing VBIT-4:lipid ratios (0, 1:16, 1:8, 1:3, 1:1.5). Lipid biophysical properties of MOM mimic membranes were evaluated in the presence of increasing VBIT-4 concentrations, either in the charged (red) or neutral (blue) form, as well as a 50:50 mixture of both states (orange). We monitored several indicators of membrane integrity: **G.** Area per lipid, **H.** Bilayer thickness, **I.** POPC acyl-chain order (membrane packing and organization), **J.** Lipid tail protrusion (packing defects), **K.** Bilayer water crossing (membrane permeability), and **L.** Lipid flip-flop (bilayer asymmetry). Each system was simulated for 10 µs in triplicate, and error bars represent the standard deviation across replicates. **M.** Potential of Mean Force (PMF) profiles for polar defect formation in coarse-grained MOM membrane systems, shown as a function of the pore formation reaction coordinate ξ, for membranes without VBIT-4 (black), with charged VBIT-4 (red), and with neutral VBIT-4 (blue). Curve uncertainty (under the single-digit kJ mol^{-1} range) is represented by shading in the same colours along the corresponding curve. **N.** Representative snapshots of the membrane systems in the presence of neutral VBIT along the reaction coordinate; lipid PO_4 beads are represented in orange, cholesterol ROH in dark orange, water beads in blue (only those in the vicinity of the lipid headgroups or the established defect are shown), and VBIT-4 in grey.

VBIT-4 increases membrane permeability and cytotoxicity in HeLa cells

Given VBIT-4 membrane-disrupting effects, its partitioning into membranes could potentially contribute to cellular cytotoxicity. We assessed its cytotoxicity in live HeLa wild-type (WT) and VDAC1 knockout (KO) cell lines using the multitox-fluor multiplex cytotoxicity assay kit that reports on both membrane integrity and cell viability. In intact cells, the live-cell protease cleaves cell-permeant GF-AFC, leading to AFC fluorescence. Loss of membrane integrity leads to inactivation of live-cell protease and the release of dead-cell proteases, which can cleave the cell-impermeant bis-AAF-R110 and increase R110 fluorescence. This dual-measurement approach provides a comprehensive evaluation of the cytotoxic effects of VBIT-4, allowing us to directly correlate membrane disruption with cellular damage. There is a decrease in AFC fluorescence and an increase in R110 fluorescence above 10 µM VBIT-4 with an IC_{50} of ~25-30 µM for HeLa WT and VDAC1 KO cell lines (**Figure 5A**). This suggests that the action of VBIT-4 on HeLa cells is independent of VDAC1, consistent with the loss of membrane integrity and corroborating our previous finding that VBIT-4 can perturb membranes and form pores above 10 µM irrespective of VDAC1.

We expect VBIT-4 to partition into multiple cellular membranes; however, because of highly negative mitochondrial membrane potential, they are likely to preferentially attract the positively charged VBIT-4, prompting us to assess its effects on mitochondrial function. VBIT-4 reduced oxygen consumption rate (OCR) in a concentration-dependent manner (**Figure 5B**) within 6 hours of treatment. VBIT-4 also decreases the mitochondrial calcium measured with Rhod-2 dye (**Figure 5C)**, mitochondrial membrane potential measured with TMRM **(Figure 5D)**, without affecting mitochondrial mass (MTG) (**Supplementary Figure 7A**), as previously reported[44, 45]. Normalization of TMRM to MTG further confirmed a significant loss of mitochondrial potential at 10 µM VBIT-4 (**Figure 5E**). These results could be explained by the membrane-destabilization activity observed in our in vitro experiments with VBIT-4. Notably, the efficacy of VBIT-4 appeared to be dependent on storage conditions. Long-term storage at -20 °C results in complete loss of activity within two months, and even storage at -80 °C, leads to reduced efficacy compared to freshly prepared solutions (**Supplementary Figure 7B**). VBIT-4 is described by different

manufacturers as an unstable molecule (one month at -20°C, see the storage and stability information in selleckchem.com or other manufacturers). This could explain the inconsistencies in various publications. Our observations emphasize the importance of using VBIT-4 fresh samples.

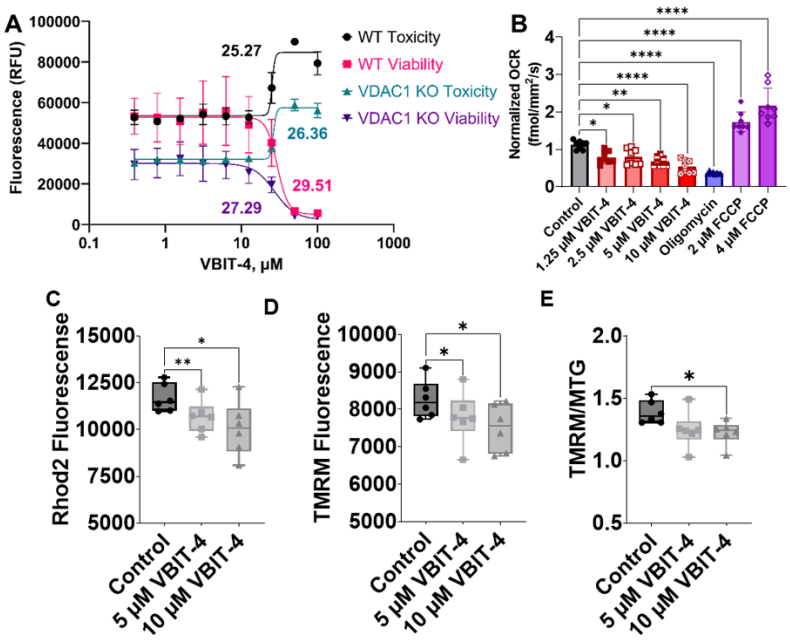

Figure 5. VBIT-4 decreases cell viability, mitochondrial respiration, and mitochondrial membrane potential in HeLa cells. A. The graph shows a decrease in viability and an increase in cytotoxicity with increasing concentration of VBIT-4 in WT and VDAC1 KO HeLa cells. The data represent the average of quadruplicate measurements, and the error bars represent the standard deviation. The corresponding IC_{50} for VBIT-4 are shown next to the nonlinear regression fitting curves. **B**. Bar graphs represent changes in the mitochondrial oxygen consumption rate (OCR) after 6 hours of treatment with 1.25 -10 μM VBIT-4 (red square symbols) compared to DMSO control (●) normalized to OCR before drug treatment. HeLa cells were treated with 0.5 μM oligomycin (▲), 2 μM (♦), and 4 μM FCCP (◊) as positive controls. Symbols represent 8 replicates, and error bars represent the standard deviation from the mean. Flow cytometry measurements of mitochondrial calcium using Rhod-2 (**C**) and mitochondrial membrane potential using TMRM **(D)** upon the addition of 5 μM (■) and 10 μM (▲) VBIT-4 compared to vehicle control (●). **E.** TMRM fluorescence normalized to MTG fluorescence (TMRM/MTG). Data from 6 independent experiments are represented in the box plots. The symbols represent data from independent experiments. The borders of the boxes define the 25th and 75th percentiles, with the median displayed as black lines and error bars indicating the standard deviation from the mean. Significance was tested using one-way ANOVA followed by the Dunnett post hoc test (*$p < 0.05$, **$p < 0.01$, ***$p<0.001$, ****$p<0.0001$).

Discussion

VBIT-4 was introduced in 2016 as a selective inhibitor of VDAC1 oligomerization, proposed to directly bind VDAC1 and prevent apoptosis triggered by cisplatin or selenite[19]. Since then, it has

been widely adopted as a probe for VDAC1-dependent pathways in diverse disease contexts, including neurodegeneration, autoimmunity, and cancer[13, 46–49]. However, its mechanism of action was not well understood. Using a combination of biophysical methods and in vitro approaches, our results fundamentally challenge the interpretation of the assumed mechanism of action of VBIT-4. Across a suite of complementary approaches—HS-AFM, microscale thermophoresis, electrophysiology, laurdan fluorescence, liposome-leakage assays, and molecular dynamic simulations—we consistently observed that VBIT-4 partitions into lipid bilayers and destabilizes them. VBIT-4 inserts into protein-free regions, drives lipid flip-flop, increases the area per lipid, reduces bilayer thickness, and promotes water permeation and the formation of pore-like defects. At micromolar concentrations—used in most cell-based studies—these perturbations become prominent and occur in different lipid environments, independently of VDAC1, as shown by three independent techniques (AFM, electrophysiology, and MST). Consistent with its membrane-disruptive activity, VBIT-4 exerts cytotoxicity in the micromolar range as previously reported[45]. We observed increased cell death in WT and VDAC1 KO HeLa cells, establishing that VBIT-4 toxicity is independent of VDAC1. The increased dead-cell protease activity, measured using a cell-impermeant fluorophore, suggests membrane permeabilization at concentrations greater than 10 µM VBIT-4. These findings demonstrate that VBIT-4 does not act as a specific VDAC1 inhibitor but rather functions as a membrane-active compound whose effects derive from general lipid membrane disruption (**Figure 6**).

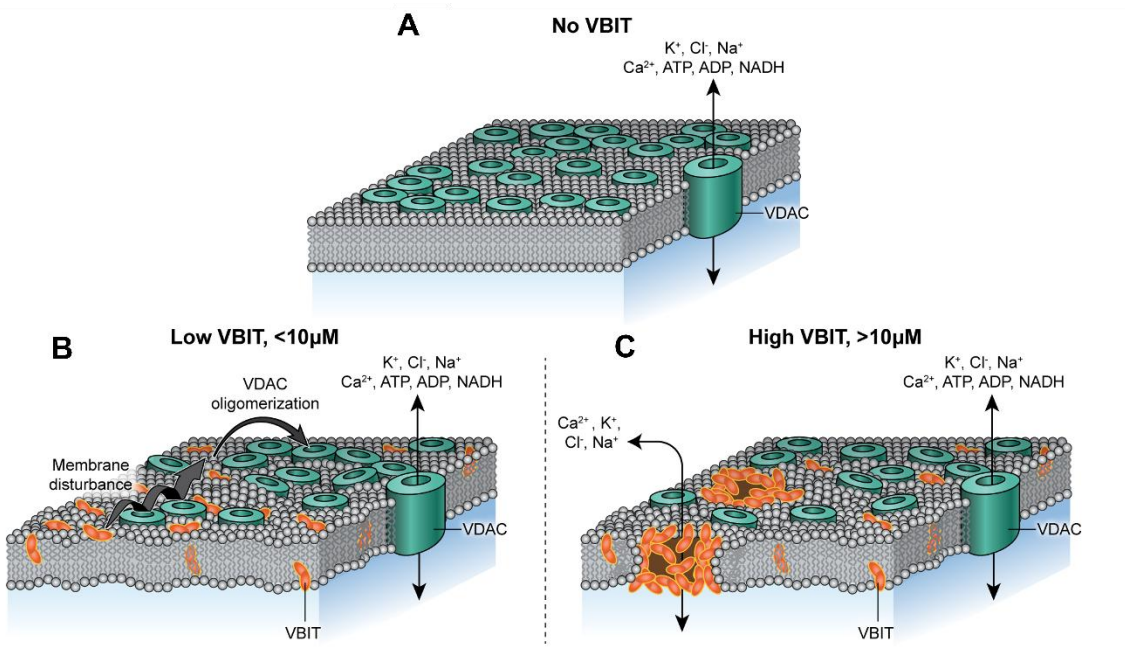

Figure 6. Putative model of VBIT-4 partitioning into a VDAC1-containing lipid membrane and VBIT-4 pore formation. A. Without VBIT-4, VDAC1 forms clusters of different sizes and compactions with both direct and lipid-mediated contacts between VDAC1 β-barrels. **B**. At low concentrations (< 10 µM), VBIT-4 partitions into the membrane, destabilizing it, which could lead to a change in compaction of VDAC1 clusters. **C**. At high concentrations (>10 µM), VBIT-4 forms water-soluble pores in the membrane, inducing membrane permeabilization, further affecting membrane integrity, which can affect VDAC1 clusters, highly sensitive to membrane composition. Direct contacts between VDAC1 β-barrels could be lost, with a few layers of lipids detected in

421 between VDAC1 β-barrels. In all three scenarios, VDAC1 monomers maintain their transport
422 channel properties, conducting the water-soluble metabolites, such as ATP, ADP, and NADH, and
423 small ions, including calcium.

424

425 At concentrations below 10 μM, VBIT-4 decreased mitochondrial calcium, respiration, and
426 membrane potential in HeLa cells without affecting mitochondrial mass, as previously reported
427 [44, 45]. These findings indicate organelle dysfunction rather than targeted VDAC1 channel
428 inhibition. They align with reports that VBIT-4 accumulates in the mitochondrial inner membrane,
429 where it inhibits respiratory complexes I, III, and IV and decreases mitochondrial membrane
430 potential[44, 45]. Notably, Belosludtsev et al. observed a decrease in calcium retention capacity at
431 30 μM VBIT-4 in their experiments on isolated mitochondria, which may indicate that VBIT-4 is
432 a mitochondrial pore inducer. However, VBIT-4 also reduced the rate of calcium-dependent
433 organelle swelling. This discrepancy was attributed to depolarization of the mitochondrial inner
434 membrane, which inhibits both mitochondrial calcium retention and mitochondrial swelling[44].

435 All above raises concerns regarding the inconsistencies in published cell data where VBIT-4 was
436 used: while some studies report clear toxicity above 10–20 μM (our data and [45]), others describe
437 apparent protection in pathological settings[13, 19, 50]. The variability can be attributed to various
438 factors. First, the behaviour of VBIT-4 is strongly influenced by its poor chemical stability—
439 consistent with our observation that cytotoxicity disappears after only two months of storage in
440 DMSO at −20 °C (**Supplementary Figure 7B**). Second, this reinterpretation is supported by its
441 physicochemical profile: with two ionizable nitrogens in the piperazine ring, VBIT-4 exists at
442 physiological pH as neutral and monocationic species that both display poor solubility, aggregation,
443 and strong membrane partitioning. As a consequence, the effective intracellular concentration of
444 VBIT-4 could vary notably with pH, storage conditions, and formulation, contributing to
445 substantial variability across research groups. Third, most studies use VBIT-4 at ~10 μM—below
446 overt cytotoxicity yet within the range where membrane perturbation occurs—and typically assess
447 its effects in combination with apoptosis inducers or in disease models rather than measuring direct
448 toxicity. Such discrepancies likely reflect differences in assay sensitivity, compound handling, and
449 pH, as well as the altered membrane composition of diseased cells. In this context, "protective"
450 effects are more plausibly attributed to nonspecific modulation of cellular membrane (including
451 mitochondrial membrane) properties than to inhibition of VDAC1 oligomerization.

452 VDAC1 oligomerization has been proposed to regulate mitochondrial DNA release[13], lipid
453 scrambling[14], and apoptosis[51], making it an attractive but controversial therapeutic target, as
454 the implications of blocking VDAC1 oligomerization remain poorly understood. Yet, the structural
455 basis of these assemblies remains elusive: except for a few defined interfaces[52–54], VDAC1 does
456 not form rigid, stoichiometric oligomers but rather heterogeneous lipid–protein clusters[1, 2, 17,
457 18] whose size and compaction are strongly lipid-dependent[17]. Cross-linking—the assay most
458 commonly used to monitor VDAC1 "oligomerization"—therefore does not report on oligomer
459 number or stability but rather on the proximity of proteins within these adaptable clusters in MOM.
460 The organization of VDAC1 in the MOM is extremely sensitive to lipid composition[17]; any
461 hydrophobic compound that perturbs membrane properties can alter cross-linking efficiency.
462 VBIT-4, even at low concentration, modifies lipid packing, and the reduced cross-linking observed
463 in treated cells could be explained by cluster expansion and loss of tight protein–protein contacts,
464 rather than by disruption of VDAC1 assemblies (see **Supplementary Fig. 8** for schematic changes
465 in cluster organization and direct contacts, **Figure 6 B,C**). Such effects should not be interpreted

466 as inhibition of VDAC1 oligomerization. In most publications, the effect of VBIT-4 on VDAC1
467 oligomerization was observed and quantified exclusively as VDAC1 dimerization[13, 19, 21, 50,
468 55]. Considering the proposed VDAC1 dimer scrambles activity[14], VBIT-4 treatment could
469 affect lipid exchange between two mitochondrial membranes (e.g., cardiolipin transfer) and
470 MAMs, leading to multiple consequences in the cell. Membrane perturbations could also affect
471 VDAC's interaction with ER calcium channels, thereby decreasing mitochondrial calcium
472 overload, which is known to lead to apoptosis. Thus, the decrease in mitochondrial calcium could
473 be linked to the protective effect of VBIT-4 at lower concentrations in pathological models.
474 Consequently, the prevailing view of VBIT-4 as a specific VDAC1 inhibitor requires re-evaluation,
475 as its cellular activity is more consistent with nonspecific modulation of the lipid environment.

476 Importantly, VBIT-4 does not selectively target MOM; it first traverses and perturbs the plasma
477 membrane, potentially disrupting other cellular membranes. By altering lipid organization, VBIT-
478 4 is poised to influence numerous pathways beyond VDAC1, including calcium transport, electron
479 transport chain function, and apoptosis—consistent with reports showing that it perturbs respiratory
480 complexes in the inner mitochondrial membrane[45].

481 The nonspecific membrane activity of VBIT-4 highlights a broader challenge in drug discovery for
482 membrane proteins. Hydrophobic small molecules frequently partition into bilayers, where they
483 can alter lipid organization. Some drugs exert dominant, target-specific effects that justify their use.
484 In the case of VBIT-4, however, all our assays—high-speed AFM, electrophysiology, microscale
485 thermophoresis, and cytotoxicity—showed no detectable effect on VDAC1 itself. Instead, all
486 observed effects are best explained by VBIT-4–induced membrane disruption, independent of
487 VDAC1, a behavior that can obscure mechanistic interpretation when protein selectivity is
488 assumed. Well-documented cases include licofelone, a COX/5-LOX inhibitor whose clinical
489 development failed partly due to off-target membrane disruption[56], and omeprazole, which
490 intercalates into DPPC bilayers and alters lipid domain structure[57].

491 Taken together, these findings demonstrate that VBIT-4 is not a reliable drug against VDAC1
492 oligomerization. Our results therefore caution against interpreting VBIT-4–induced phenotypes as
493 evidence of VDAC1 inhibition. Systematic assessment of drug–membrane interactions early in
494 development is therefore essential, as the absence of rigorous lipid-only controls can result in
495 membrane-driven effects being erroneously attributed to specific protein inhibition.

496 # Materials and Methods

497 **VBIT-4**

498 VBIT-4 was purchased from Selleck Chemicals (VBIT-4, Cat. No.S3544,Selleckchem, Houston,
499 TX, dissolved in DMSO for biophysical experiments, in powder for cytotoxicity assays) and stored
500 at −80 °C according to the manufacturer's instructions. Aliquots were used within one year of
501 purchase.

502 **mVDAC1 purification**

503 mVDAC1 production and purification were performed as previously described[58]. A pQE9
504 plasmid encoding mouse VDAC1 with an N-terminal 6×His tag was expressed as inclusion bodies
505 in *Escherichia coli* M15 (pREP4) cells (Creative Biolabs). Cells were grown at 37 °C with agitation
506 until reaching an OD_{600} of 0.7, and protein expression was induced for 4 h with 1 mM IPTG. Cells

were harvested by centrifugation and resuspended in 50 mM Tris-HCl pH 8.0, 2 mM EDTA, and 20% (w/v) sucrose. Lysis was performed by lysozyme treatment followed by sonication. Inclusion bodies were isolated by centrifugation for 15 min at 12,000 × *g*, washed with 20 mM Tris-HCl pH 8.0, 300 mM NaCl, and 2 mM $CaCl_2$, and solubilized in 20 mM Tris-HCl pH 8.0, 300 mM NaCl, and 8 M urea for 1 h. Insoluble material was removed by centrifugation at 25,000 × *g* for 1 h.

The supernatant containing solubilized mVDAC1 was loaded onto a Ni–NTA affinity column and eluted with 20 mM Tris-HCl pH 8.0, 300 mM NaCl, 8 M urea, and 150 mM imidazole. The purified protein was refolded by rapid dilution into 20 mM Tris-HCl pH 8.0, 150 mM NaCl, 10 mM DTT, and 1.5% (w/v) LDAO. Refolded protein was ultracentrifuged at 355,000 × *g* for 45 min to remove aggregates, concentrated, and further purified by size-exclusion chromatography on a Superdex 200 Increase 10/300 GL column (Fig. S11). The monomeric VDAC peak was collected, concentrated to 2 mg/mL, flash-frozen in liquid nitrogen, and stored in 20% (v/v) glycerol at −80 °C. Samples were ultracentrifuged after thawing prior to liposome reconstitution to remove residual aggregates.

Reconstitution into liposomes

POPE, POPC, and cholesterol (Avanti Polar Lipids) were mixed in chloroform at 62.5:30:7.5 molar ratios and dried under a nitrogen stream. The lipid film was resuspended in 150 mM KCl, 20 mM Tris (pH 8.0) to a final lipid concentration of 12.5 mg/mL and vortexed thoroughly. The suspension was incubated at 37 °C for 10 min and sonicated for 1 min, or until small unilamellar vesicles (~100 nm) formed, as verified by dynamic light scattering (DLS). For the VDAC1-containing liposmes, β-Octyl glucoside (β-OG) was added at a detergent-to-lipid ratio of 0.65 (w/w), followed by the addition of protein at a lipid-to-VDAC ratio of 3:1 (w/w). Detergent removal was performed overnight using Bio-Beads (Bio-Beads-to-detergent ratio 30:1 w/w). The resulting proteoliposomes were analyzed by DLS after reconstitution.

AFM and HS-AFM data acquisition

To prepare protein-containing supported lipid bilayers (SLBs), 15 µL of proteoliposome suspension (1 mg/mL) was mixed with 85 µL of incubation buffer (10 mM HEPES pH 7.4, 100 mM NaCl, 15 mM $CaCl_2$) and incubated for 1 h at room temperature on freshly cleaved mica under a humid hood. The samples were rinsed ten times with ultrapure water (Milli-Q) and imaged in imaging buffer (10 mM HEPES pH 7.4, 100 mM NaCl, 5 mM $CaCl_2$) at 35 °C to verify membrane homogeneity. All conditions were tested in triplicate.

Conventional AFM imaging was performed in contact mode using a Nanoscope IIIe Multimode AFM (Bruker, Santa Barbara, CA, USA) equipped with OTR4 probes (k = 0.1 N/m). The scan rate, feedback gains, and deflection setpoint were adjusted during acquisition to optimize image quality. HS-AFM imaging was carried out in amplitude-modulation mode using a modified high-speed AFM (SS-NEX, RIBM, Tsukuba, Japan) optimized for molecular-resolution imaging[59]. The instrument was equipped with a custom digital high-speed lock-in amplifier coded on a reconfigurable FPGA platform using LabVIEW (National Instruments, Austin, TX, USA). Short cantilevers (~7 µm) designed for HS-AFM and fitted with electron-beam-deposited (EBD) tips were used (USC-F1.2-k0.15, Nanoworld, Switzerland). These cantilevers have a nominal spring constant of 0.15 N/m, a resonance frequency in liquid of ~500 kHz, and a quality factor (Q) of ~2. The deflection sensitivity was 0.1 V/nm, and the imaging amplitude setpoint was ~90% of the free amplitude (~10 Å). All HS-AFM experiments were performed at 35 °C inside a temperature-controlled enclosure.

552 **Image analysis**

553 Acquired images were plane-fit and flattened using the AFM processing and analysis software
554 provided by the instrument manufacturer. HS AFM image treatment was limited to the correction
555 of XY drift and a first-order X-line fit. Image analysis was performed using the general distribution
556 of ImageJ[60] and of WSxM[61].

557 **Preparation of nanodiscs**

558 MSP1D1 membrane scaffold protein was produced and purified as described by Ritchie, T. K. et
559 al.[62]. Chloroform-solubilised lipids (Chicken egg phosphatidylcholine) were dried under
560 nitrogen gas and re-solubilised in 20 mM Tris pH 8.0 buffer containing 50mM sodium cholate at a
561 final concentration of 25 mM lipid. Lipids and MSP were mixed at a 65:1 molar ratio at 4°C for 1
562 hour. Bio-Beads SM2 were added at a 50x excess (weight) of total detergent, and the mix was
563 incubated overnight at 4 °C on agitation. The nanodiscs were filtered through a 0.2 µm sterile
564 syringe filter and centrifuged at 100,000 x g for 30 minutes at 4 °C. The supernatant was subjected
565 to size exclusion chromatography on a Superdex 200 increase 10/300 GL column in 20 mM HEPES
566 pH 7.4, 100 mM NaCl. The nanodisc-containing fractions were concentrated for labelling.
567 Nanodiscs were labelled using the Protein Labelling Kit RED-NHS 2nd Generation from
568 NanoTemper (NT-L021) at a 1:1.5 protein:dye molar ratio in 20 mM HEPES buffer pH 7.4, 100
569 mM NaCl for 2 hours at 4°C in the dark. Excess dye was removed using a Micro Bio-Spin P6
570 column equilibrated in the same buffer. The degree of labelling was determined using UV-Vis
571 spectrophotometry at 650 nm and 280 nm according to the manufacturer's instructions. The degree
572 of labelling was between 60-75% ($\varepsilon_{nanodisc}$ = 36,900 M^{-1} cm^{-1}, ε_{dye} = 195,000 M^{-1} cm^{-1}) across the
573 replicates.

574

575 **Preparation of VDAC1 nanodiscs**

576 mVDAC1 was purified and refolded as explained above, except the final gel filtration was
577 performed in 20mM HEPES buffer pH 7.4, 100mM NaCl, 0.1% LDAO. Detergent-refolded
578 VDAC1 was labelled using the Protein Labelling Kit RED-NHS 2nd Generation from NanoTemper
579 (NT-L021) at a 1:1.5 protein:dye molar ratio for 2 hours at 4°C in the dark. Excess dye was removed
580 using a Micro Bio-Spin P6 column equilibrated in the gel filtration buffer. The degree of labelling
581 was determined using UV-Vis spectrophotometry at 650 nm and 280 nm according to the
582 manufacturer's instructions. The degree of labelling was 30% (ε_{VDAC1} = 43,890 M-1 cm-1, εdye =
583 195,000 M-1 cm-1). Labelled VDAC1 was reconstituted into MSP1D1 nanodiscs by incubating
584 proteins with cholate-solubilised lipids (EggPC) at a 65:1 molar ratio lipids:MSP and 12:1 molar
585 ratio MSP:VDAC1 for 1 hour at 4°C before adding 50x excess (wt) of BioBeads SM2 and
586 incubating overnight at 4 °C on agitation. The nanodiscs were filtered through a 0.2 µm sterile
587 syringe filter and centrifuged at 100,000 x g for 30 minutes at 4 °C. The supernatant was subjected
588 to size exclusion chromatography on a Superdex 200 increase 10/300 GL column in 20 mM HEPES
589 pH 7.4, 100 mM NaCl. Reconstituted VDAC1 was concentration in an Amicon-50 and used in
590 MST experiments.

591

592 **Microscale Thermophoresis (MST)**

MST experiments were performed using a NanoTemper Monolith X MO-G039, Munich, Germany. VBIT-4 (Selleckchem #S3544) was diluted in DMSO at a final concentration of 10 mM and sub-stocks of 1 mM were made in buffer 20 mM HEPES pH 7.4, 100 mM NaCl containing 10 % DMSO. 15 µL of 50nM labelled nanodiscs or VDAC1-containing nanodiscs were incubated with 15 µL of VBIT-4 (0.25 - 500 µM) and incubated for 20 minutes at room temperature as performed by Ben-Hail et. al.[17]. Following a short tabletop spin, 10 µL of the samples were loaded into 12 glass capillaries (NanoTemper premium capillaries, MO-K022) and thermophoresis was performed (60% excitation power at 650nm, and a medium infra-red laser power with a wavelength of 1480nm). The final concentration of DMSO in the capillaries was maintained at 5%. Thermophoresis experiments were performed as described by the manufacturer and data were analysed at 650 nm at a laser ON-time of 2.5s since they had the best SNR (Signal to Noise Ratio. Data were fitted by the system.

Laurdan generalised polarisation

Laurdan-containing liposomes were prepared by mixing chloroform-solubilized lipids (PC:PE:Chol, 62.5:30:7.5) at a concentration of 1 mM total lipids with chloroform-solubilized laurdan at a lipid:laurdan molar ratio of 1000:1. Lipid mixtures were dried under nitrogen gas in the dark. Liposomes were formed by resuspending dried lipids in 200 µL of 20 mM HEPES buffer pH 7.4 containing 100 mM NaCl and vortexing. Liposomes were sonicated with 10 pulses at 10% power, 10% ON/OFF cycle to form SUVs with an average diameter of 100 nm as verified by dynamic light scattering. Laurdan-containing liposomes were diluted 10x in buffer and added to a quartz cuvette (pathlength 3 mm) at a final volume of 150 µL. Sub-stocks of VBIT-4 in DMSO were made such that the final volume added to the cuvette would be a constant 1 µL. Control samples contained the same volume of DMSO. The excitation wavelength was set to 375 nm and the emission scan range was from 400-600 nm. Excitation slit width – 10 nm, emission slit width – 5 nm. Data were recorded at a scanning speed of 600 nm/min at 26 °C on a Cary Eclipse fluorescence spectrometer. Generalised polarisation was calculated as $GP = (I_{440} - I_{490}) / (I_{440} + I_{490})$. GP was plotted as a function of VBIT-4 concentration on Python using a partitioning model.

Planar lipid bilayer measurements

Planar lipid membranes (PLM) were formed by two different techniques: 1) using "dry" membranes formed by the lipid monolayer opposition technique on a circular aperture in a Teflon partition dividing two ~1.5 mL (*cis* and *trans*) compartments of the experimental chamber, as previously described[63], and 2) using "painted" membranes from lipid solution in decane using Orbit mini system (Nanion Technologies, Minich, Germany)[64]. Lipids dioleoyl-phosphatidylcholine (DOPC), dioleoyl-phosphatidylethanolamine (DOPE), diphytanoyl-phosphatidylcholine (DPhPC), polar lipid extract from soybean (PLE), and cholesterol (Avanti Polar Lipids) were used for PLM preparations. Aqueous solutions consisted of 150 mM KCl buffered with 5 mM HEPES at pH 7.4. In the first method of PLM formation, the 5 mg/mL lipid mixtures in pentane were used. The aperture in the Teflon partition was pretreated by 1% hexadecane in pentane before PLM formation, thus leaving only a residual amount of hexadecane in the bilayers. The current recordings were performed as described previously[63], using Axopatch 200B amplifier (Axon Instruments) in the voltage-clamp mode. Data were filtered by a low-pass 8-pole Butterworth filter (Model 900 Frequency Active Filter, Frequency Devices) at 15 kHz,

digitized with a sampling frequency of 50 kHz, and analysed using pClamp 10.7 software (Axon Instrument). For data analysis, digital filtering using a 1 or 0.5 kHz low-pass Bessel filter was applied. Potential is defined as positive when it is greater on the *cis* side, the side of VBIT-4 and VDAC1 addition. In the second method, lipid bilayers were formed by painting the chips (Ionera, Freiburg, Germany) with the 5 mg/mL lipid mixtures in decane. Multi Electrode Cavity Array (MECA4) chips were filled with 150 µL of 150 mM KCl solution at pH 7.4. VBIT-4 in DMSO solution was added to the bilayer in both experimental setups after PLM was formed, and its conductance of less than 0.1 pS was verified. VBIT-4 in DMSO solution was added to the bilayer in both experimental setups after PLM was formed, up to a total volume of less than 5 uL, and PLM conductance of less than 0.1 pS was verified. Addition of the corresponding DMSO aliquots to the membrane-bathing solutions did not change membrane conductance[65]. All measurements were performed at room temperature of 21 ± 1ºC.

VDAC conductance measurements

Recombinant mouse VDAC1 was expressed, refolded, and purified as described previously[66]. Channel insertion was achieved by adding 0.1-1.5 mL of VDAC diluted in buffer containing 10 mM Tris, 50 mM KCl, 1 mM EDTA, 15 % (v/v) DMSO, 2.5% (v/v) Triton X-100, pH 7.0. Current recording and its analysis were performed as described previously[67]. VDAC1 voltage-gating properties were assessed following the previously described protocol [68] under the application of a slow symmetrical 5 mHz triangular voltage wave of ±60 mV amplitude from an Arbitrary Waveform Generator 33220A (Agilent). Data were acquired at a sampling frequency of 2 Hz and analyzed as described previously[68] using an algorithm developed in-house and pClamp 10.7 software. In each experiment, current records were collected from membranes containing 10-50 channels in response to 5–10 periods of voltage waves to ensure data collection from more than 50 channels per experiment. Only the part of the wave, during which the channels were reopening, was used for the subsequent analysis[69].

Liposome leakage assay

Liposomes (PC:PE:chol, 62.5:30:7.5 w:w) were prepared by mixing 5mg of chloroform-solubilized lipids in a glass tube. Dried lipids were resuspended in 200 µL of 100 mM fluorescein dissolved in HEPES buffer pH 7.4, and vortexed vigorously. Liposomes were subjected to 3 cycles of freeze-thawing in liquid nitrogen followed by 50°C in a Thermomix. Liposomes were then sonicated with 20 pulses at 20% power, 10% ON/OFF cycle to form SUVs of diameter 50-100 nm as verified by dynamic light scattering. Liposomes were pelleted by centrifugation at 25,000 rpm for 30 mins at 4°C on a TLA55 rotor. The supernatant was discarded, and liposomes were washed with 1 mL of HEPES buffer. The washing/centrifugation step was repeated till no free fluorescein was detectible by absorbance spectroscopy. Pelleted liposomes were resuspended in 1 mL of HEPES buffer, and 32 µL of liposomes were used in each 200 µL reaction in a 96-well plate, giving a final concentration of 1 mM lipid/reaction. Sub-stocks of VBIT-4 in DMSO were made such that the final volume added to each well would be a constant 1 µL. The negative control sample included 1 µL of DMSO, while the positive control sample included 1 µL of 100% Triton X-100. Time-resolved fluorescence spectra were recorded in a Tecan Spark plate reader for 2 hours every 30 seconds with shaking between each reading. Excitation and emission wavelengths for fluorescein were set to 485 nm and 535 nm, respectively. At the end of the kinetics, 1 µL of Triton X-100 was added to solubilise the liposomes. Data were normalised w.r.t. liposomes treated with DMSO as $F_{norm} = (F-F_{min})/(F_{max} - F_{min})$ after 100 min, and a histogram of % release was plotted.

VBIT-4 CG parameterization

VBIT-4 charge state. VBIT-4 contains a piperazine group with two nitrogen atoms. These are typically protonable under physiological conditions, with pKa values usually in the range of 7–9. Out of these two, the most protonable nitrogen is the one closer to the hydroxyl (-OH) and amide (-CONH-) groups. The nitrogen near the benzene ring is both sterically hindered and electronically less basic due to the $-OCF_3$ group's electron-withdrawing effect. The nitrogen near the amide and hydroxyl is both more exposed and more basic, making it the preferred protonation site. Given the significant conformational differences observed between the neutral and protonated versions of VBIT-4 in our reference AA simulations, we developed a Martini CG model for each state and analyzed their effects separately.

All-atom reference simulations. VBIT-4 Martini 3 models were based on simulations of all-atom counterparts, parameterized using the OPLS-AA force field via LigParGen[70–72]. Each system was simulated for 500 ns in water. Each system was minimized using steepest descent with 5000 steps, followed by a relaxation of 250 ps using a 1 fs time step, and a production run of 500 ns using a 2 fs time step. The temperature and pressure were held constant at 298 K and 1 bar using the Berendsen thermostat and barostat[73] for the relaxation step and the V-rescale thermostat[74] and Parrinello-Rahman barostat[75] for the production run. The pressure coupling was isotropic with a compressibility of 4.5×10^{-5} bar^{-1}. The temperature was coupled using $\tau = 1$ ps during both the relaxation and production run. For pressure coupling, $\tau = 1$ ps was set during relaxation and 5 ps during production. The electrostatics were treated with the PME algorithm[76] using a cutoff of 1.2 nm, while the van der Waals interactions were truncated, smoothly switching the force to zero between 1.0 and 1.2 nm[77]. Bonds involving hydrogen atoms were restricted using the LINCS algorithm[78].

Coarse-grained model parameterization. Martini CG models were then obtained according to the parametrization rules of Martini 3, as described elsewhere[79]. In short, atomistic simulations were mapped into CG resolution using MD Analysis[80, 81] . The bonded terms were then measured and the distributions plotted. The molecule was then modelled in CG and simulated in water. Bonded distributions were fitted onto the corresponding atomistic distributions. Bead types and sizes were selected according to Martini 3 parametrization guidelines, ensuring consistency with default bead assignments for specific chemical groups[79]. These choices were validated by estimating CG octanol/water partitioning free energies, which were compared to predictors obtained via SwissADME[82] (iLOGP[83], XLOGP3[84], WLOGP[85], MLOGP[86], SILICOS-IT). The calculated partitioning free energies were obtained by thermodynamic integration as described elsewhere[79].

VBIT-4 Martini CG MD Simulations

Unbiased CG MD. Membrane bilayers were constructed with COBY[87], which also solvated the system, neutralized it, and added ions to obtain a 150 mM NaCl concentration. COBY also added the appropriate number of VBIT-4 molecules in solution. All systems were subject to the same relaxation and production protocol. First, a minimization of 5000 steps using steepest descent, followed by 10 ns of relaxation, and finally at least 5 μs production run. A complex membrane composition mimicking the mitochondrial outer membrane was used

(8:25:17:13:4:9:3:8:4 CHOL:POPC:DOPC:DPPC:POPE:DOPE:DPPE:POPS:POPI:DPPI) in a 15 × 15 × 17.5 nm^3 system. Prior to production, the systems underwent 5000 energy minimization steps, followed by equilibration for 10 ns using a 10 fs time step. During equilibration, VBIT-4 molecules were pulled into the membrane using flat-bottom potentials to avoid sampling the membrane adsorption process. These potentials were not applied during the production run. The production runs for each system were carried out for 10 µs. Throughout the simulations, the temperatures of the lipids (including VBIT-4) and solvent (including ions) were independently maintained at 300 K using the v-rescale thermostat (τ_t = 1 ps)[74], and the pressure was kept at 1 bar using the c-rescale barostat (τ_p = 4 ps)[88] with semi-isotropic pressure coupling applied during both equilibration and production phases. Compressibility was set to 3×10^{-4} bar^{-1}. As suggested by Kim et al.[89], the cut-off distance for the short-range neighbor list was set to 1.35 nm for proper neighbor list updates.

Membrane translocation PMF. Similarly to the unbiased CG MD systems, COBY was used to build a smaller 7 × 7 × 13.5 nm^3 system, fully solvated with water and 150 mM NaCl. One VBIT-4 molecule was placed 4 nm away (determined from the center of geometry of VBIT-4) from the bilayer center along the bilayer normal, and overlapping water molecules were removed. Minimization and equilibration were performed as with the unbiased simulations. At the end of the equilibration, initial configurations for the umbrella sampling windows were generated by pulling the VBIT-4 molecule through the bilayer center at a rate of 0.0001 nm/ps and a force constant of 3000 kJ/mol/nm^2. In each umbrella sampling window, a harmonic potential was applied to keep the VBIT-4 molecule in its pre-defined distance from the bilayer center with a force constant ranging from 1000 to 2000 kJ/mol/nm^2. A total of 52 windows were simulated for 2 µs and the data from the first 200 ns were discarded before applying the weighted histogram analysis method to estimate the free energy profile using GROMACS. The translocation PMF of the molecule was computed along the entire membrane normal from z = 5.25 to z = -5.25. For each replica, the PMF was symmetrized by splitting it at the membrane center and averaging both halves. The final PMF and standard deviation were obtained by averaging the symmetrized profiles across all replicas.

Polar defect formation PMF. Polar defect formation PMF was determined as described by Hub and Awasthi[43]. Small 10 × 10 × 14 nm^3 membrane bilayer systems were built using COBY, as described for the unbiased MD systems. Minimization and equilibration were performed as with the unbiased simulations. The initial frames for the umbrella sampling simulations were extracted from constant velocity pulling simulations. In these simulations, the systems were pulled from the reaction chain coordinate[43, 90] ξ_{ch} = 0.25 to ξ_{ch} = 1 over 1000 ns using a force constant of 5000 kJ mol^{-1}. Nineteen umbrella windows were employed, with reference positions ranging from ξch = 0.1 to 1 in increments of 0.05, where 1 is the fully formed pore. The force constant was set to 8000 kJ mol^{-1}. Each window was simulated for 1 μs, with the initial 500 ns excluded for equilibration. Three replicas of each window were run. The potential of mean force was computed using the weighted histogram analysis method (WHAM)[91].

Cell toxicity assay

HeLa WT and VDAC1 knockout cells from Synthego were seeded at 2,500 cells/well in a 96-well plate (ThermoFisher Scientific, 165305) in DMEM (Gibco, 15607) supplemented with 10% FBS (Gibco, 10437). 200 mM VBIT-4 was prepared by adding 54.6 µL DMSO to 5 mg VBIT-4 (Selleckchem.com, S3544) and was added to the cells at a final concentration of 0-200 µM VBIT-4. After 48 hours at 37 °C and 5% CO_2, GF-AFC and bis-AAF-R110 substrates from the MultiTox-

771 Fluor Multiplex Cytotoxicity Assay kit (Promega, G9201) were added to the cells following the
772 manufacturer's protocol and incubated for 30 minutes at 37 °C. Viability and cytotoxicity were
773 measured using 400/505 nm and 485/520 nm excitation/emission filters, respectively, in a
774 CLARIOstar plate reader. Nonlinear regression curve fit was applied to calculate the IC_{50} for VBIT-
775 4 using GraphPad Prism (version 10.1.2).

776 **Mitochondrial oxygen consumption rate measurement.**

777 HeLa cells were seeded in a 96-well plate at 10,000 cells/well in DMEM with 10% FBS and the
778 oxygen consumption rate (OCR) were measured with Resipher device (Lucid Scientific, Atlanta,
779 GA, USA). Baseline OCR was measured overnight before treatment with vehicle control, 1.25 to
780 10 µM VBIT-4, 0.5 µM Oligomycin, 2 µM and 4 µM FCCP. OCR data after 6 hours of
781 incubation with drugs were normalized to the baseline OCR for each well.

782 **Mitochondrial mass, membrane potential, and calcium measurements by flow cytometry**

783 HeLa cells were seeded into 24-well plates at $1x10^5$ cells/well in DMEM with 10% FBS. Cells
784 were mock-treated or treated with 5 µM or 10 µM VBIT-4 overnight (16 hours). Trypsinized cells
785 were washed and loaded with Mitotracker Green for flow cytometry (MTG, 0.5 µl/ml for
786 mitochondrial mass) and tetramethylrhodamine methyl ester (TMRM, 10 nM, for membrane
787 potential) in PBS for 30 minutes at 37 °C with Live/Dead Near-IR dye added for the last 15 minutes.
788 Alternatively, cells were stained with Rhod2-AM (1 µM, calcium indicator) and 0.02% Pluronic
789 F-127 in PBS for 1 hour at room temperature, washed and resuspended in 250 µL of PBS and
790 incubated at room temperature for 30 minutes with Live/Dead Near-IR dye added for the last 15
791 minutes (all reagents from Thermo Fisher). Cells were acquired on a BD FACSymphony A5 with
792 TMRM or Rhod2 signal acquired in YG 586/15, MTG acquired in Blue 530/30, and live cell dye
793 in Red 780/60. Analysis was performed in FlowJo 10.10 (Becton Dickinson) with cell gate
794 established by forward scatter versus side scatter, followed by singlet gate, live cell gate, and
795 determination of mean fluorescence intensity of MTG, TMRM, or Rhod2.

796 **FTIR**

797 A Bruker TENSOR FT-IR spectrophotometer equipped with an ATR plate and an MCT D316
798 nitrogen-cooled detector was used to further characterize the VBIT-4 IR absorption band and the
799 pH-dependent solubility of the molecule. A VBIT-4 suspension containing 10 µL of VBIT at 25
800 mg/mL in DMSO, 20 µL of H_2O, and 10 µL of HCl (0.03%) is prepared just prior to the experiment.
801 Four µL of the slightly turbid suspension is deposited on the surface of the diamond plate and
802 equilibrated for 15 minutes with a cover slip to avoid evaporation. At this point, the upper liquid is
803 adsorbed using the capillarity of a cleaning paper, and the surface is washed twice using 4 µL of
804 50 mM phosphate buffer (pH 7.6) and 100 mM NaCl.

805 This procedure is sufficient to completely remove the FTIR signal of DMSO and shows a strong
806 adsorption of VBIT-4 on the diamond surface, as depicted by two characteristic areas of absorption
807 bands in the 1470-1570 cm^{-1} and 1125-1300 cm^{-1} regions. From this starting situation, we
808 characterize the tendency of the adsorbed VBIT-4 to elute using phosphate buffer (pH 7.6).

809

810 **Acknowledgements**

We thank Dr. Manuel N. Melo for the insightful suggestion that inspired the polar defect formation simulations. This work was supported by the Aix-Marseille Université grant AMX-21-PEP-022 (L.B.) and a PhD fellowship from Aix-Marseille Université (V.R.). L.B.A. acknowledges the support of the French National Centre for Scientific Research and the HPC resources provided by IDRIS, CINES, and TGCC through GENCI (allocation 2024-A0160713456). L.B.A. also acknowledges the support of the Centre Blaise Pascal de Simulation et Modélisation Numérique's IT test platform at ENS de Lyon (Lyon, France) for the computer facilities. M.S.W., W.F., N.A.B., B.G.B., M.G.L., M.R., S.M.B., and T.K.R. acknowledge the support of the Intramural Research Program of the National Institutes of Health (NIH), *Eunice Kennedy Shriver* National Institute of Child Health and Human Development (NICHD). This research was supported in part by the Intramural Research Program of the National Institutes of Health (NIH). The contributions of the NIH authors are considered Works of the United States Government. The findings and conclusions presented in this paper are those of the authors and do not necessarily reflect the views of the NIH or the U.S. Department of Health and Human Services.

References

1. Gonçalves RP, Buzhynskyy N, Prima V, Sturgis JN, Scheuring S (2007) Supramolecular assembly of VDAC in native mitochondrial outer membranes. J Mol Biol 369:413–418. https://doi.org/10.1016/j.jmb.2007.03.063

2. Hoogenboom BW, Suda K, Engel A, Fotiadis D (2007) The supramolecular assemblies of voltage-dependent anion channels in the native membrane. J Mol Biol 370:246–255. https://doi.org/10.1016/j.jmb.2007.04.073

3. Naghdi S, Várnai P, Hajnóczky G (2015) Motifs of VDAC2 required for mitochondrial Bak import and tBid-induced apoptosis. Proc Natl Acad Sci U S A 112:E5590-5599. https://doi.org/10.1073/pnas.1510574112

4. Yuan Z, Dewson G, Czabotar PE, Birkinshaw RW (2021) VDAC2 and the BCL-2 family of proteins. Biochem Soc Trans 49:2787–2795. https://doi.org/10.1042/BST20210753

5. Sander P, Gudermann T, Schredelseker J (2021) A Calcium Guard in the Outer Membrane: Is VDAC a Regulated Gatekeeper of Mitochondrial Calcium Uptake? Int J Mol Sci 22:946. https://doi.org/10.3390/ijms22020946

6. Shankar TS, Ramadurai DKA, Steinhorst K, Sommakia S, Badolia R, Thodou Krokidi A, Calder D, Navankasattusas S, Sander P, Kwon OS, Aravamudhan A, Ling J, Dendorfer A, Xie C, Kwon O, Cheng EHY, Whitehead KJ, Gudermann T, Richardson RS, Sachse FB, Schredelseker J, Spitzer KW, Chaudhuri D, Drakos SG (2021) Cardiac-specific deletion of voltage dependent anion channel 2 leads to dilated cardiomyopathy by altering calcium homeostasis. Nat Commun 12:4583. https://doi.org/10.1038/s41467-021-24869-0

7. Rosencrans WM, Rajendran M, Bezrukov SM, Rostovtseva TK (2021) VDAC regulation of mitochondrial calcium flux: From channel biophysics to disease. Cell Calcium 94:102356. https://doi.org/10.1016/j.ceca.2021.102356

8. Queralt-Martín M, Bergdoll L, Teijido O, Munshi N, Jacobs D, Kuszak AJ, Protchenko O, Reina S, Magrì A, De Pinto V, Bezrukov SM, Abramson J, Rostovtseva TK (2020) A lower affinity to cytosolic proteins reveals VDAC3 isoform-specific role in mitochondrial biology. J Gen Physiol 152:. https://doi.org/10.1085/jgp.201912501

9. Xu X, Decker W, Sampson MJ, Craigen WJ, Colombini M (1999) Mouse VDAC isoforms expressed in yeast: channel properties and their roles in mitochondrial outer membrane permeability. J Membr Biol 170:89–102. https://doi.org/10.1007/s002329900540

10. Camara AKS, Zhou Y, Wen P-C, Tajkhorshid E, Kwok W-M (2017) Mitochondrial VDAC1: A Key Gatekeeper as Potential Therapeutic Target. Front Physiol 8:460. https://doi.org/10.3389/fphys.2017.00460

11. Magri A, Messina A (2017) Interactions of VDAC with Proteins Involved in Neurodegenerative Aggregation: An Opportunity for Advancement on Therapeutic Molecules. Curr Med Chem 24:4470–4487. https://doi.org/10.2174/0929867324666170601073920

12. Reina S, De Pinto V (2017) Anti-Cancer Compounds Targeted to VDAC: Potential and Perspectives. Curr Med Chem 24:4447–4469. https://doi.org/10.2174/0929867324666170530074039

13. Kim J, Gupta R, Blanco LP, Yang S, Shteinfer-Kuzmine A, Wang K, Zhu J, Yoon HE, Wang X, Kerkhofs M, Kang H, Brown AL, Park S-J, Xu X, Zandee van Rilland E, Kim MK, Cohen JI, Kaplan MJ, Shoshan-Barmatz V, Chung JH (2019) VDAC oligomers form mitochondrial pores to release mtDNA fragments and promote lupus-like disease. Science 366:1531–1536. https://doi.org/10.1126/science.aav4011

14. Jahn H, Bartoš L, Dearden GI, Dittman JS, Holthuis JCM, Vácha R, Menon AK (2023) Phospholipids are imported into mitochondria by VDAC, a dimeric beta barrel scramblase. Nat Commun 14:8115. https://doi.org/10.1038/s41467-023-43570-y

15. Leung MR, Zenezini Chiozzi R, Roelofs MC, Hevler JF, Ravi RT, Maitan P, Zhang M, Henning H, Bromfield EG, Howes SC, Gadella BM, Heck AJR, Zeev-Ben-Mordehai T (2021) In-cell structures of conserved supramolecular protein arrays at the mitochondria-cytoskeleton interface in mammalian sperm. Proc Natl Acad Sci U S A 118:e2110996118. https://doi.org/10.1073/pnas.2110996118

16. Callegari S, Kirk NS, Gan ZY, Dite T, Cobbold SA, Leis A, Dagley LF, Glukhova A, Komander D (2025) Structure of human PINK1 at a mitochondrial TOM-VDAC array. Science 388:303–310. https://doi.org/10.1126/science.adu6445

17. Lafargue E, Duneau J-P, Buzhinsky N, Ornelas P, Ortega A, Ravishankar V, Sturgis J, Casuso I, Bergdoll L (2025) Membrane lipid composition modulates the organization of VDAC1, a mitochondrial gatekeeper. Commun Biol 8:936. https://doi.org/10.1038/s42003-025-08311-5

888 18. Mannella CA, Colombini M, Frank J (1983) Structural and functional evidence for multiple
889 channel complexes in the outer membrane of Neurospora crassa mitochondria. Proc Natl
890 Acad Sci U S A 80:2243–2247. https://doi.org/10.1073/pnas.80.8.2243

891 19. Ben-Hail D, Begas-Shvartz R, Shalev M, Shteinfer-Kuzmine A, Gruzman A, Reina S, De Pinto
892 V, Shoshan-Barmatz V (2016) Novel Compounds Targeting the Mitochondrial Protein
893 VDAC1 Inhibit Apoptosis and Protect against Mitochondrial Dysfunction. J Biol Chem
894 291:24986–25003. https://doi.org/10.1074/jbc.M116.744284

895 20. Klapper-Goldstein H, Verma A, Elyagon S, Gillis R, Murninkas M, Pittala S, Paul A, Shoshan-
896 Barmatz V, Etzion Y (2020) VDAC1 in the diseased myocardium and the effect of VDAC1-
897 interacting compound on atrial fibrosis induced by hyperaldosteronism. Sci Rep 10:22101.
898 https://doi.org/10.1038/s41598-020-79056-w

899 21. Verma A, Shteinfer-Kuzmine A, Kamenetsky N, Pittala S, Paul A, Nahon Crystal E, Ouro A,
900 Chalifa-Caspi V, Pandey SK, Monsonego A, Vardi N, Knafo S, Shoshan-Barmatz V (2022)
901 Targeting the overexpressed mitochondrial protein VDAC1 in a mouse model of
902 Alzheimer's disease protects against mitochondrial dysfunction and mitigates brain
903 pathology. Transl Neurodegener 11:58. https://doi.org/10.1186/s40035-022-00329-7

904 22. Belosludtsev KN, Serov DA, Ilzorkina AI, Starinets VS, Dubinin MV, Talanov EY, Karagyaur
905 MN, Primak AL, Belosludtseva NV (2023) Pharmacological and Genetic Suppression of
906 VDAC1 Alleviates the Development of Mitochondrial Dysfunction in Endothelial and
907 Fibroblast Cell Cultures upon Hyperglycemic Conditions. Antioxidants (Basel) 12:1459.
908 https://doi.org/10.3390/antiox12071459

909 23. Mohammad Al-Amily I, Sjögren M, Duner P, Tariq M, Wollheim CB, Salehi A (2023) Ablation
910 of GPR56 Causes β-Cell Dysfunction by ATP Loss through Mistargeting of Mitochondrial
911 VDAC1 to the Plasma Membrane. Biomolecules 13:557.
912 https://doi.org/10.3390/biom13030557

913 24. Wei S-N, Zhang H, Lu Y, Yu H-J, Ma T, Wang S-N, Yang K, Tian M-L, Huang A-H, Wang W, Li F-
914 S, Li Y-W (2023) Microglial voltage-dependent anion channel 1 signaling modulates sleep
915 deprivation-induced transition to chronic postsurgical pain. Sleep 46:zsad039.
916 https://doi.org/10.1093/sleep/zsad039

917 25. Luo X, Yue J (2025) VDAC1 Inhibition Mitigates Inflammatory Status and Oxidative Stress in
918 Epileptic Mice Treated with the Ketogenic Diet. Neurochem Res 50:118.
919 https://doi.org/10.1007/s11064-025-04366-2

920 26. Terrones O, Antonsson B, Yamaguchi H, Wang H-G, Liu J, Lee RM, Herrmann A, Basañez G
921 (2004) Lipidic Pore Formation by the Concerted Action of Proapoptotic BAX and tBID.
922 Journal of Biological Chemistry 279:30081–30091.
923 https://doi.org/10.1074/jbc.M313420200

924 27. Colombini M (2019) Ceramide Channels. In: Stiban J (ed) Bioactive Ceramides in Health and
925 Disease. Springer International Publishing, Cham, pp 33–48

926 28. Anosov AA, Smirnova EYu, Ryleeva ED, Gligonov IA, Korepanova EA, Sharakshane AA (2020)
927 Estimation of the parameters of the Smoluchowski equation describing the occurrence of
928 pores in a bilayer lipid membrane under soft poration. Eur Phys J E 43:66.
929 https://doi.org/10.1140/epje/i2020-11989-0

930 29. Steringer JP, Bleicken S, Andreas H, Zacherl S, Laussmann M, Temmerman K, Contreras FX,
931 Bharat TAM, Lechner J, Müller H-M, Briggs JAG, García-Sáez AJ, Nickel W (2012)
932 Phosphatidylinositol 4,5-Bisphosphate (PI(4,5)P2)-dependent Oligomerization of Fibroblast
933 Growth Factor 2 (FGF2) Triggers the Formation of a Lipidic Membrane Pore Implicated in
934 Unconventional Secretion. Journal of Biological Chemistry 287:27659–27669.
935 https://doi.org/10.1074/jbc.M112.381939

936 30. Ashrafuzzaman M, Tseng C, Duszyk M, Tuszynski JA (2012) Chemotherapy Drugs Form Ion
937 Pores in Membranes Due to Physical Interactions with Lipids. Chem Biol Drug Des 80:992–
938 1002. https://doi.org/10.1111/cbdd.12060

939 31. Perini DA, Aguilella-Arzo M, Alcaraz A, Perálvarez-Marín A, Queralt-Martín M (2022)
940 Dynorphin A induces membrane permeabilization by formation of proteolipidic pores.
941 Insights from electrophysiology and computational simulations. Computational and
942 Structural Biotechnology Journal 20:230–240. https://doi.org/10.1016/j.csbj.2021.12.021

943 32. Serra-Batiste M, Ninot-Pedrosa M, Bayoumi M, Gairí M, Maglia G, Carulla N (2016) Aβ42
944 assembles into specific β-barrel pore-forming oligomers in membrane-mimicking
945 environments. Proc Natl Acad Sci USA 113:10866–10871.
946 https://doi.org/10.1073/pnas.1605104113

947 33. Gorny H, Mularoni A, Delcros J-G, Freton C, Preto J, Krimm I (2023) Combining nano-
948 differential scanning fluorimetry and microscale thermophoresis to investigate VDAC1
949 interaction with small molecules. J Enzyme Inhib Med Chem 38:2121821.
950 https://doi.org/10.1080/14756366.2022.2121821

951 34. Souza PCT, Alessandri R, Barnoud J, Thallmair S, Faustino I, Grünewald F, Patmanidis I,
952 Abdizadeh H, Bruininks BMH, Wassenaar TA, Kroon PC, Melcr J, Nieto V, Corradi V, Khan
953 HM, Domański J, Javanainen M, Martinez-Seara H, Reuter N, Best RB, Vattulainen I,
954 Monticelli L, Periole X, Tieleman DP, de Vries AH, Marrink SJ (2021) Martini 3: a general
955 purpose force field for coarse-grained molecular dynamics. Nat Methods 18:382–388.
956 https://doi.org/10.1038/s41592-021-01098-3

957 35. Bieker S, Timme M, Woge N, Hassan DG, Brown CM, Marrink SJ, Melo MN, Holthuis JCM
958 (2024) Hexokinase-I directly binds to a charged membrane-buried glutamate of
959 mitochondrial VDAC1 and VDAC2. 2024.07.22.604557

960 36. Dadsena S, Bockelmann S, Mina JGM, Hassan DG, Korneev S, Razzera G, Jahn H, Niekamp P,
961 Müller D, Schneider M, Tafesse FG, Marrink SJ, Melo MN, Holthuis JCM (2019) Ceramides
962 bind VDAC2 to trigger mitochondrial apoptosis. Nat Commun 10:1832.
963 https://doi.org/10.1038/s41467-019-09654-4

964 37. Mazzobre MF, Román MV, Mourelle AF, Corti HR (2005) Octanol-water partition coefficient
965 of glucose, sucrose, and trehalose. Carbohydr Res 340:1207–1211.
966 https://doi.org/10.1016/j.carres.2004.12.038

967 38. Fornasier F, Souza LMP, Souza FR, Reynaud F, Pimentel AS (2020) Lipophilicity of Coarse-
968 Grained Cholesterol Models. J Chem Inf Model 60:569–577.
969 https://doi.org/10.1021/acs.jcim.9b00830

970 39. Avdeef A (1993) pH-metric log P. II: Refinement of partition coefficients and ionization
971 constants of multiprotic substances. J Pharm Sci 82:183–190.
972 https://doi.org/10.1002/jps.2600820214

973 40. MolGpka: A Web Server for Small Molecule pKa Prediction Using a Graph-Convolutional
974 Neural Network | Journal of Chemical Information and Modeling.
975 https://pubs.acs.org/doi/abs/10.1021/acs.jcim.1c00075. Accessed 3 Dec 2025

976 41. Creyf HS, Van Poucke LC (1972) The free energy, enthalpy and entropy changes of the
977 dissociation of diprotonated diamines. Thermochimica Acta 4:485–491.
978 https://doi.org/10.1016/0040-6031(72)85039-1

979 42. Pedersen KB, Ingólfsson HI, Ramirez-Echemendia DP, Borges-Araújo L, Andreasen MD,
980 Empereur-Mot C, Melcr J, Ozturk TN, Bennett DW, Kjølbye LR, others (2024) The Martini 3
981 lipidome: expanded and refined parameters improve lipid phase behavior

982 43. Hub JS, Awasthi N (2017) Probing a Continuous Polar Defect: A Reaction Coordinate for Pore
983 Formation in Lipid Membranes. J Chem Theory Comput 13:2352–2366.
984 https://doi.org/10.1021/acs.jctc.7b00106

985 44. Belosludtsev KN, Serov DA, Ilzorkina AI, Starinets VS, Dubinin MV, Talanov EY, Karagyaur
986 MN, Primak AL, Belosludtseva NV (2023) Pharmacological and Genetic Suppression of
987 VDAC1 Alleviates the Development of Mitochondrial Dysfunction in Endothelial and
988 Fibroblast Cell Cultures upon Hyperglycemic Conditions. Antioxidants (Basel) 12:1459.
989 https://doi.org/10.3390/antiox12071459

990 45. Belosludtsev KN, Ilzorkina AI, Matveeva LA, Chulkov AV, Semenova AA, Dubinin MV,
991 Belosludtseva NV (2024) Effect of VBIT-4 on the functional activity of isolated
992 mitochondria and cell viability. Biochim Biophys Acta Biomembr 1866:184329.
993 https://doi.org/10.1016/j.bbamem.2024.184329

994 46. Taniguchi H, Chakraborty S, Takahashi N, Banerjee A, Caeser R, Zhan YA, Tischfield SE, Chow
995 A, Nguyen EM, Villalonga ÁQ, Manoj P, Shah NS, Rosario S, Hayatt O, Qu R, de Stanchina E,
996 Chan J, Mukae H, Thomas A, Rudin CM, Sen T (2024) ATR inhibition activates cancer cell
997 cGAS/STING-interferon signaling and promotes antitumor immunity in small-cell lung
998 cancer. Science Advances 10:eado4618. https://doi.org/10.1126/sciadv.ado4618

999 47. Bround MJ, Havens JR, York AJ, Sargent MA, Karch J, Molkentin JD (2023) ANT-dependent
1000 MPTP underlies necrotic myofiber death in muscular dystrophy. Science Advances
1001 9:eadi2767. https://doi.org/10.1126/sciadv.adi2767

1002 48. Zhang E, Al-Amily IM, Mohammed S, Luan C, Asplund O, Ahmed M, Ye Y, Ben-Hail D, Soni A,
1003 Vishnu N, Bompada P, Marinis YD, Groop L, Shoshan-Barmatz V, Renström E, Wollheim CB,
1004 Salehi A (2019) Preserving Insulin Secretion in Diabetes by Inhibiting VDAC1
1005 Overexpression and Surface Translocation in β Cells. Cell Metabolism 29:64-77.e6.
1006 https://doi.org/10.1016/j.cmet.2018.09.008

1007 49. Gulen MF, Samson N, Keller A, Schwabenland M, Liu C, Glück S, Thacker VV, Favre L,
1008 Mangeat B, Kroese LJ, Krimpenfort P, Prinz M, Ablasser A (2023) cGAS-STING drives ageing-
1009 related inflammation and neurodegeneration. Nature 620:374–380.
1010 https://doi.org/10.1038/s41586-023-06373-1

1011 50. Baik SH, Ramanujan VK, Becker C, Fett S, Underhill DM, Wolf AJ (2023) Hexokinase
1012 dissociation from mitochondria promotes oligomerization of VDAC that facilitates NLRP3
1013 inflammasome assembly and activation. Science Immunology 8:eade7652.
1014 https://doi.org/10.1126/sciimmunol.ade7652

1015 51. Keinan N, Tyomkin D, Shoshan-Barmatz V (2010) Oligomerization of the mitochondrial
1016 protein voltage-dependent anion channel is coupled to the induction of apoptosis. Mol
1017 Cell Biol 30:5698–5709. https://doi.org/10.1128/MCB.00165-10

1018 52. Bergdoll LA, Lerch MT, Patrick JW, Belardo K, Altenbach C, Bisignano P, Laganowsky A,
1019 Grabe M, Hubbell WL, Abramson J (2018) Protonation state of glutamate 73 regulates the
1020 formation of a specific dimeric association of mVDAC1. Proc Natl Acad Sci USA 115:E172–
1021 E179. https://doi.org/10.1073/pnas.1715464115

1022 53. Schredelseker J, Paz A, López CJ, Altenbach C, Leung CS, Drexler MK, Chen J-N, Hubbell WL,
1023 Abramson J (2014) High resolution structure and double electron-electron resonance of
1024 the zebrafish voltage-dependent anion channel 2 reveal an oligomeric population. J Biol
1025 Chem 289:12566–12577. https://doi.org/10.1074/jbc.M113.497438

1026 54. Takeda H, Shinoda S, Goto C, Tsutsumi A, Sakaue H, Zhang C, Hirashima T, Konishi Y, Ono H,
1027 Yamamori Y, Tomii K, Shiino H, Tamura Y, Zuttion S, Senger B, Friant S, Becker HD, Araiso Y,
1028 Kobayashi N, Kodera N, Kikkawa M, Endo T (2025) Oligomer-based functions of
1029 mitochondrial porin. Nat Commun 16:. https://doi.org/10.1038/s41467-025-62021-4

1030 55. Oflaz FE, Bondarenko AI, Trenker M, Waldeck-Weiermair M, Gottschalk B, Bernhart E,
1031 Koshenov Z, Radulović S, Rost R, Hirtl M, Pilic J, Karunanithi Nivedita A, Sagintayev A,
1032 Leitinger G, Brachvogel B, Summerauer S, Shoshan-Barmatz V, Malli R, Graier WF (2025)
1033 Annexin A5 controls VDAC1-dependent mitochondrial Ca2+ homeostasis and determines
1034 cellular susceptibility to apoptosis. EMBO J 44:3413–3447.
1035 https://doi.org/10.1038/s44318-025-00454-9

1036 56. Pereira-Leite C, Lopes-de-Campos D, Fontaine P, Cuccovia IM, Nunes C, Reis S (2019)
1037 Licofelone-DPPC Interactions: Putting Membrane Lipids on the Radar of Drug
1038 Development. Molecules 24:516. https://doi.org/10.3390/molecules24030516

1039 57. Lopes-de-Campos D, Pereira-Leite C, Fontaine P, Coutinho A, Prieto M, Sarmento B,
1040 Jakobtorweihen S, Nunes C, Reis S (2021) Interface-Mediated Mechanism of Action-The
1041 Root of the Cytoprotective Effect of Immediate-Release Omeprazole. J Med Chem
1042 64:5171–5184. https://doi.org/10.1021/acs.jmedchem.1c00251

1043 58. Dearden GI, Ravishankar V, Sakata K-T, Menon AK, Bergdoll L (2024) Protocol for the
1044 production and reconstitution of VDAC1 for functional assays. STAR Protoc 5:103240.
1045 https://doi.org/10.1016/j.xpro.2024.103240

1046 59. Ando T, Kodera N, Takai E, Maruyama D, Saito K, Toda A (2001) A high-speed atomic force
1047 microscope for studying biological macromolecules. Proc Natl Acad Sci U S A 98:12468–
1048 12472. https://doi.org/10.1073/pnas.211400898

1049 60. Schneider CA, Rasband WS, Eliceiri KW (2012) NIH Image to ImageJ: 25 years of image
1050 analysis. Nat Methods 9:671–675. https://doi.org/10.1038/nmeth.2089

1051 61. Horcas I, Fernández R, Gómez-Rodríguez JM, Colchero J, Gómez-Herrero J, Baro AM (2007)
1052 WSXM: a software for scanning probe microscopy and a tool for nanotechnology. Rev Sci
1053 Instrum 78:013705. https://doi.org/10.1063/1.2432410

1054 62. Ritchie TK, Grinkova YV, Bayburt TH, Denisov IG, Zolnerciks JK, Atkins WM, Sligar SG (2009)
1055 Chapter 11 - Reconstitution of membrane proteins in phospholipid bilayer nanodiscs.
1056 Methods Enzymol 464:211–231. https://doi.org/10.1016/S0076-6879(09)64011-8

1057 63. Rostovtseva TK, Kazemi N, Weinrich M, Bezrukov SM (2006) Voltage gating of VDAC is
1058 regulated by nonlamellar lipids of mitochondrial membranes. J Biol Chem 281:37496–
1059 37506. https://doi.org/10.1074/jbc.M602548200

1060 64. Narahari AK, Kreutzberger AJ, Gaete PS, Chiu Y-H, Leonhardt SA, Medina CB, Jin X, Oleniacz
1061 PW, Kiessling V, Barrett PQ, Ravichandran KS, Yeager M, Contreras JE, Tamm LK, Bayliss DA
1062 (2021) ATP and large signaling metabolites flux through caspase-activated Pannexin 1
1063 channels. Elife 10:e64787. https://doi.org/10.7554/eLife.64787

1064 65. Rostovtseva TK, Weinrich M, Jacobs D, Rosencrans WM, Bezrukov SM (2024) Dimeric
1065 Tubulin Modifies Mechanical Properties of Lipid Bilayer, as Probed Using Gramicidin A
1066 Channel. International Journal of Molecular Sciences 25:2204.
1067 https://doi.org/10.3390/ijms25042204

1068 66. Ujwal R, Cascio D, Colletier J-P, Faham S, Zhang J, Toro L, Ping P, Abramson J (2008) The
1069 crystal structure of mouse VDAC1 at 2.3 A resolution reveals mechanistic insights into
1070 metabolite gating. Proc Natl Acad Sci U S A 105:17742–17747.
1071 https://doi.org/10.1073/pnas.0809634105

1072 67. Queralt-Martín M, Bergdoll L, Jacobs D, Bezrukov SM, Abramson J, Rostovtseva TK (2019)
1073 Assessing the role of residue E73 and lipid headgroup charge in VDAC1 voltage gating.
1074 Biochim Biophys Acta Bioenerg 1860:22–29. https://doi.org/10.1016/j.bbabio.2018.11.001

1075 68. Teijido O, Rappaport SM, Chamberlin A, Noskov SY, Aguilella VM, Rostovtseva TK, Bezrukov
1076 SM (2014) Acidification asymmetrically affects voltage-dependent anion channel
1077 implicating the involvement of salt bridges. J Biol Chem 289:23670–23682.
1078 https://doi.org/10.1074/jbc.M114.576314

1079 69. Rappaport SM, Teijido O, Hoogerheide DP, Rostovtseva TK, Berezhkovskii AM, Bezrukov SM
1080 (2015) Conductance hysteresis in the voltage-dependent anion channel. Eur Biophys J
1081 44:465–472. https://doi.org/10.1007/s00249-015-1049-2

1082 70. Dodda LS, Cabeza de Vaca I, Tirado-Rives J, Jorgensen WL (2017) LigParGen web server: an
1083 automatic OPLS-AA parameter generator for organic ligands. Nucleic Acids Res 45:W331–
1084 W336. https://doi.org/10.1093/nar/gkx312

1085 71. Dodda LS, Vilseck JZ, Tirado-Rives J, Jorgensen WL (2017) 1.14*CM1A-LBCC: Localized Bond-
1086 Charge Corrected CM1A Charges for Condensed-Phase Simulations. J Phys Chem B
1087 121:3864–3870. https://doi.org/10.1021/acs.jpcb.7b00272

1088 72. Jorgensen WL, Tirado-Rives J (2005) Potential energy functions for atomic-level simulations
1089 of water and organic and biomolecular systems. Proc Natl Acad Sci U S A 102:6665–6670.
1090 https://doi.org/10.1073/pnas.0408037102

1091 73. Berendsen HJC, Postma JPM, van Gunsteren WF, Di Nola A, Haak JR (1984) Molecular
1092 dynamics with coupling to an external bath. Journal of Chemical Physics 81:3684–3690.
1093 https://doi.org/10.1063/1.448118

1094 74. Bussi G, Donadio D, Parrinello M (2007) Canonical sampling through velocity rescaling. J
1095 Chem Phys 126:014101. https://doi.org/10.1063/1.2408420

1096 75. Parrinello M, Rahman A (1981) Polymorphic transitions in single crystals: A new molecular
1097 dynamics method. Journal of applied physics 7182–7190

1098 76. Darden T, York D, Pedersen L (1993) Particle mesh Ewald: An N·log(N) method for Ewald
1099 sums in large systems. Journal of Chemical Physics 10089–10092

1100 77. Páll S, Hess B (2013) A flexible algorithm for calculating pair interactions on SIMD
1101 architectures. Computer Physics Communications 184:2641–2650.
1102 https://doi.org/10.1016/j.cpc.2013.06.003

1103 78. Hess B, Bekker H, Berendsen HJC, Fraaije JGEM (1997) LINCS: A linear constraint solver for
1104 molecular simulations. Journal of Computational Chemistry 18:1463–1472.
1105 https://doi.org/10.1002/(SICI)1096-987X(199709)18:12%3C1463::AID-JCC4%3E3.0.CO;2-H

1106 79. Souza PCT, Thallmair S, Conflitti P, Ramírez-Palacios C, Alessandri R, Raniolo S, Limongelli V,
1107 Marrink SJ (2020) Protein-ligand binding with the coarse-grained Martini model. Nat
1108 Commun 11:3714. https://doi.org/10.1038/s41467-020-17437-5

1109 80. Gowers RJ, Linke M, Barnoud J, Reddy TJE, Melo MN, Seyler SL, Domanski J, Dotson DL,
1110 Buchoux S, Kenney IM, Beckstein O (2019) MDAnalysis: A Python Package for the Rapid
1111 Analysis of Molecular Dynamics Simulations. In: Report Number: LA-UR-19-29136.
1112 Research Org.: Los Alamos National Laboratory (LANL), Los Alamos, NM (United States)

1113 81. Michaud-Agrawal N, Denning EJ, Woolf TB, Beckstein O (2011) MDAnalysis: a toolkit for the
1114 analysis of molecular dynamics simulations. J Comput Chem 32:2319–2327.
1115 https://doi.org/10.1002/jcc.21787

1116 82. Daina A, Michielin O, Zoete V (2017) SwissADME: a free web tool to evaluate
1117 pharmacokinetics, drug-likeness and medicinal chemistry friendliness of small molecules.
1118 Sci Rep 7:42717. https://doi.org/10.1038/srep42717

1119 83. Daina A, Michielin O, Zoete V (2014) iLOGP: a simple, robust, and efficient description of n-
1120 octanol/water partition coefficient for drug design using the GB/SA approach. J Chem Inf
1121 Model 54:3284–3301. https://doi.org/10.1021/ci500467k

1122 84. Cheng T, Zhao Y, Li X, Lin F, Xu Y, Zhang X, Li Y, Wang R, Lai L (2007) Computation of octanol-
1123 water partition coefficients by guiding an additive model with knowledge. J Chem Inf
1124 Model 47:2140–2148. https://doi.org/10.1021/ci700257y

1125 85. Wildman SA, Crippen GM (1999) Prediction of Physicochemical Parameters by Atomic
1126 Contributions. Journal of Chemical Information and Computer Sciences 39:868–873.
1127 https://doi.org/10.1021/ci990307l

1128 86. Lipinski CA, Lombardo F, Dominy BW, Feeney PJ (2001) Experimental and computational
1129 approaches to estimate solubility and permeability in drug discovery and development
1130 settings. Adv Drug Deliv Rev 46:3–26. https://doi.org/10.1016/s0169-409x(00)00129-0

1131 87. Andreasen MD, Souza PCT, Schiøtt B, Zuzic L (2024) Creating Coarse-Grained Systems with
1132 COBY: Towards Higher Accuracy in Membrane Complexity. bioRxiv.
1133 https://doi.org/10.1101/2024.07.23.604601

1134 88. Bernetti M, Bussi G (2020) Pressure control using stochastic cell rescaling. J Chem Phys
1135 153:114107. https://doi.org/10.1063/5.0020514

1136 89. Kim H, Fábián B, Hummer G (2023) Neighbor List Artifacts in Molecular Dynamics
1137 Simulations. J Chem Theory Comput 19:8919–8929.
1138 https://doi.org/10.1021/acs.jctc.3c00777

1139 90. Awasthi N, Hub JS (2019) Free-energy calculations of pore formation in lipid membranes. In:
1140 Biomembrane Simulations. CRC Press, pp 109–124

1141 91. Kumar S, Rosenberg JM, Bouzida D, Swendsen RH, Kollman PA (1992) THE weighted
1142 histogram analysis method for free-energy calculations on biomolecules. I. The method.
1143 Journal of Computational Chemistry 13:1011–1021

1144